ASTON UNIVERSITY

A PROJECT COMPLETED AS PART OF THE REQUIREMENTS FOR THE

MSc BY RESEARCH

The Study of an Inclined Internally Heated Fluid Flow

Author:

Chloe SEIVWRIGHT

Supervisor(s):

Dr. Sotos GENERALIS

Dr. Greg CARTLAND-GLOVER

October 2013

Aston University
Birmingham

Abstract

The subject of this dissertation is an analysis of fluid flow stability. Early transitions of convection are theoretically modelled when considering an internal heat source and asymmetric boundary conditions. The motivation of this study is to analyse the bifurcation sequence of the specified model. Physical properties of the flow are varied through control parameters such as: Reynolds number, Prandtl number and the angle of inclination. A number of cases are compared and numerically analysed in order to pinpoint regions where stability of the basic configuration breaks down. Furthermore, a non-linear analysis is done within the found regions in the interest of identifying further structural instabilities.

The model defined in this dissertation is applicable to a number of natural and industrial processes; the focus is to define a model that mirrors the cooling process within the shut down of a nuclear reactor. In such cases the source of the internal heat is the radioactive decay of molten nuclear fuel within the nuclear reactors. By modelling such a system, we aim to study the effects of convection with internally heated systems.

In the present study, we have identified the boundaries between a laminar and convective state for varying Prandtl number; so far we can deduce that as the Reynolds number is increased slightly, the critical Grashof number becomes more positive, suggesting that for small variations in the Reynolds number our fluid is stable in a greater region. The angle also has a similar effect for small variations, although we find when both the angle and Reynolds number are increased further this behaviour changes and the fluid in fact becomes less stable. Through the non-linear analysis performed, we identify the parameter space of the thermal flow patterns and enforce small disturbances to the states to determine their stability.

Acknowledgements

I would like to thank Dr Sotos Generalis, and Dr Greg Cartland-Glover. I would also like to give my most sincere thanks my fellow research peers, Nerupa, Larry and Jack for all of their advice and help during the more stressful periods of this year. Finally if it wasn't for the support of my family and Vernon Caisley, I would have never believed that I could overcome some of the obstacles that arose during this MSc. Their help and support over the period of this research has been invaluable.

Contents

List of Figures

List of Tables

Nomenclature

$\mathbf{u}$	-	velocity vector
∇	-	gradient $\rightarrow \left(\frac{\partial}{\partial x}, \frac{\partial}{\partial y}, \frac{\partial}{\partial z}\right)$
∇^2	-	$\left(\frac{\partial^2}{\partial x^2}, \frac{\partial^2}{\partial y^2}, \frac{\partial^2}{\partial z^2}\right)$
ρ	-	fluid density
χ	-	Angle of inclination
π	-	pressure
μ	-	dynamic viscosity
ν	-	kinematic viscosity
κ	-	thermal diffusivity
k	-	thermal conductivity
$\mathbf{g}$	-	gravitational vector force
$\mathbf{f}$	-	body force per unit mass
γ	-	thermal expansion
α	-	streamwise wave number
β	-	spanwise wave number
g	-	gravitational component
T	-	temperature
t	-	time
d	-	distance between boundaries
q	-	volume strength of heat source $\rightarrow 2\kappa\Delta T/d^2$
Δ_2	-	Planform Laplacian operator $\rightarrow (\partial_x^2 + \partial_y^2)$
δ	-	Delta operator $\rightarrow (\partial_x\partial_z, \partial_y\partial_z, -\Delta_2)$
ϵ	-	Epsilon operator $\rightarrow (\partial_y, -\partial_x, 0)$
Gr	-	Grashof number $\rightarrow g\gamma q d^5/2\nu^2\kappa$
Pr	-	Prandtl number $\rightarrow \nu/\kappa$
Ra	-	Rayleigh number $\rightarrow GrPr$
Re	-	Reynolds number $\rightarrow \frac{UL}{\nu}$

Chapter 1

Introduction

In this dissertation we define and examine the theoretical properties of an internally heated fluid in a configuration that has an insulating lower boundary and a conducting upper boundary. By varying the free parameters in the system we will explore how this effects the fluid stability. Our aim is to numerically analyse the bifurcation sequence that occurs as the fluid flow develops from laminar state to turbulent.

1.1 Motivation

Internally heated fluids arise in a number of natural and industrial processes. As a result they have become an increasingly interesting area of research. Thermal convection can be found within the Earth's core as a result of the radioactive decay. Also when exploring the atmospheric properties of a planet, flow influenced by thermal convection can be found (Schubert et al., 2001). Biochemical and chemical reactions can also heat the fluid internally as the processes involved will give off heat (Takahashi et al., 2010).

Convection due to internal heating has been studied experimentally in (Takahashi et al., 2010), (Tritton and Zarraga, 1967) where electrical currents are used to provide the internal heat source. The cell structures within the fluid layers are determined and compared while adjusting the free parameters.

Convection driven by a uniform internal heat source can also be found in corium melt pools which are used in the shut down of nuclear reactors that have undergone a severe accident (Asfia and Dhir, 1996). Nuclear fuel has been a controversial topic of discussion for many years. As the worldwide demand for energy increases, current natural resources of power (i.e. coal, natural gas) aren't sustainable, hence the need for alternative means of energy production. Nuclear fuel is undoubtedly a strong contender as an alternate solution to maintain the high global demands of power. Therefore nuclear safety is a vital element when considering such a solution. By analysing the flow structure in a model that emulates a corium melt pool, we wish to further understand the behaviour of a fluid in such a system.

1.2 The Problem

A nuclear reactor can be very basically described having a core that houses the chemical reaction that occurs. This core is encased within a thick concrete concrete chamber. When a nuclear reactor undergoes a severe accident, for example as a result of a nuclear chain reaction or heat decay, temperature levels within the core can reach up to $2000°C$. In such a situation the core of the reactor and its containing material will melt and deposit in the bottom of its containing concrete chamber as seen in Figure 1.1. The temperature difference between the concrete chamber and the molten corium fluid causes a crust to form on top of the fluid resulting in a system that has an insulating lower boundary and conducting upper boundary.

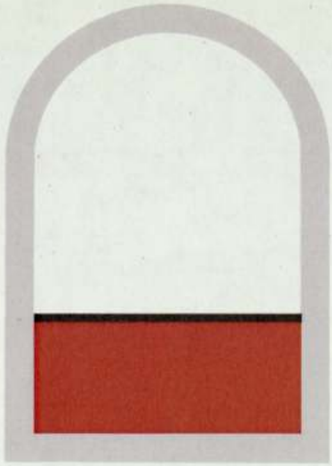

Figure 1.1: A basic sketch of a concrete chamber housing the deposited corium molten fluid. The bold black line indicates the crust formed on the molten fluid as a result of the temperature difference between the fluid and container.

A theoretical model of a system shown in Figure 1.1 will be defined in this dissertation. The aim is to adjust the free parameters for a finite number of cases in order to change the physical properties of the flow. The stability of the flow is known to be dependent on these control parameters, therefore the linear stability of the primary flow is explored by a comparative analysis of the different cases. The Chebyshev collocation method is adopted in this dissertation to approximate the linear and non-linear solutions of our specific Navier Stokes equation.

1.3 Goals and Outlines

This project focuses on pinpointing the region between stability and instability for different fluid types. The following section briefly introduces the equations and methods explored when defining the system. It explains the origin of the Navier Stokes Equations and how through a number of justified assumptions they can be simplified and solved to adhere to the study of fluid dynamics.

Chapter 3 then establishes the problem, defining the properties of the model and deriving the model-specific Navier Stokes Equation. The linear analysis of the model is then investigated in Chapter 4 where the basic temperature and flow equations are analytically derived. Numerical methods are employed to provide the linear neutral curves highlighting the boundary between laminar and convective flow. Chapter 5 investigates the non-linear analysis of the model around the neutral curve boundary. The basic non-linear solution is numerically derived and the non-linear state parameters are traced with respect to the angle of inclination. The behaviour of the strongly non-linear states are then analysed to determine their stability; whether further bifurcations occur. In Chapter 6 we discuss the conclusions of this work and consider possible future developments to further the findings of the project.

Chapter 2

Modelling a fluid

This chapter reviews the key elements that we encounter when defining the governing equations used within this study to model our fluid. A number of assumptions and approximations are made in order to best analyse specific conditions of a fluid, these will be defined and discussed.

When studying the behaviour of a dynamical system such as fluid flow, it is necessary to apply a small change known as a perturbation to the physical system to see what effect this change makes. We look to see if this small change causes instabilities in the flow that continue to grow causing chaotic property changes (Zill et al., 2009). The growth must always saturate otherwise the system explodes. The saturated state need not be turbulence, but it could lead to instabilities in the flow in which turbulent behaviour may occur.

For a multidimensional problem as defined in this dissertation, the Navier Stokes Equation is central to the problem. The equation is used to define the fluid properties of our problem. By using a collocation method, we can represent our modelled system as a set of linear equations. Eigenvalue analysis of the particular matrix corresponding to the equations is then performed to determine the stability of the state for the varying parameters. A critical point arises if the real part of the eigenvalue $\sigma_r = 0$. By analysing the critical points, we can determine the transitions from stable to unstable and vice versus. When all $\sigma_r < 0$, the system is regarded as stable, otherwise it is said to be unstable and therefore implying potential turbulent behaviour.

2.1 Navier-Stokes

To begin to mathematically construct the governing Navier-Stokes Equation, the state of a fluid must be defined. Once certain properties are characterised, the governing equations of the fluid take form. A good starting point for modelling a fluid is to consider the general laws of continuum mechanics: conservation of mass, linear momentum and energy as fluid motion satisfies these laws.

Throughout this study, we consider a Eulerian representation of a fluid, where the velocity $\mathbf{u}(\mathbf{x}, t)$ and the density $\rho(\mathbf{x}, t)$ are analysed as functions of the position $\mathbf{x}$ at a time t (Price, 2006). The model fluid can be described as Newtonian and incompressible. A Newtonian fluid is one that takes into account the stress versus strain forces by assuming them to be linearly proportional. The incompressibility condition means the density of the fluid is constant in space and time (Batchelor, 1967). The Boussinesq approximation is also followed throughout this study. These assumptions allow us to simplify the conservation equations for mass, momentum and temperature as follows.

$$\rho\left(\frac{\partial \mathbf{u}}{\partial t} + (\mathbf{u}\cdot\boldsymbol{\nabla})\mathbf{u}\right) = -\boldsymbol{\nabla}\pi + \mu\boldsymbol{\nabla}^2\mathbf{u} + \rho\mathbf{f}, \tag{2.1}$$

$$\frac{\partial T}{\partial t} + (\mathbf{u}\cdot\boldsymbol{\nabla})T = \kappa\boldsymbol{\nabla}^2 T + q, \tag{2.2}$$

$$\boldsymbol{\nabla}\cdot\mathbf{u} = 0. \tag{2.3}$$

Equations (2.1)-(2.3) represent the general momentum, temperature and incompressibility condition respectively.

2.1.1 Boussinesq Approximation

The Boussinesq approximation is a realistic simplification that can be used in most natural and industrial scenarios. It states that the density will remain constant except for the effect of gravity acting on it, therefore accounting for the buoyancy of a given fluid

(Zeytounian, 2003). This approximation follows even if a fluid moves from a region of high temperature to a low temperature. This isn't always the case when working with fluids, however with regards to the problem defined for this study, it is a viable assumption. The following equations show the relationship between the density and temperature:

$$\rho = \rho_0(1 - \gamma(T - T_0)), \tag{2.4}$$

The coefficient of volume expansion is denoted by γ. By writing the temperature at a time t as a temperature difference $T' = T - T_0$, equation (2.4) can be rewritten as follows:

$$\rho = \rho_0 - \rho_0\gamma T'. \tag{2.5}$$

For simplicity, we will write the temperature different T' as an updated temperature T.J. Boussinesq (Zeytounian, 2003) observed that, "The variations of density can be ignored except were they are multiplied by the acceleration of gravity in equation of motion for the vertical component of the velocity vector". This allows us to write equation (2.5) as follows:

$$g(\rho_0 - \rho) = -g\rho_0\gamma T. \tag{2.6}$$

By updating the momentum equation (2.1) with respect to this Boussinesq approximation, we obtain:

$$\rho_0\left(\frac{\partial \mathbf{u}}{\partial t} + (\mathbf{u}\cdot\nabla)\mathbf{u}\right) = -\nabla\pi + \mu\nabla^2\mathbf{u} - g\rho_0\gamma T, \tag{2.7}$$

we have replaced $\rho\mathbf{f}$, our external force per unit mass by $-g\rho_0\gamma T$ which will represent the buoyancy term of the Navier Stokes Equation.

2.1.2 Non-Dimensionalisation

The governing equations for the model fluid include a number of dimensional parameters. In order to solve the equations it is necessary to remove all the measured units. This allows us to solve the Navier Stokes Equations for the dimensionless case, but then apply the results to a number of scaled cases. It also simplifies the equations to a manageable number of parameters while creating control variables for the fluid transition. To nondimensionalise the governing equations, the parameters are rescaled. Each parameter needs to be normalised so that each dimensional variable can be substituted for a corresponding non-dimensional variable.

For a general case, if we have a dimensional variable x^* which has a measured unit, we can normalise this variable by dividing by a reference constant for example X. This results in a dimensionless variable x such that:

$$x = \frac{x^*}{X}.$$

This can be rearranged so we can achieve a consistent system for our dimensional variables, $x^* = Xx$. By representing each of our dimensional variables in our governing equations in such a form, we can obtain non-dimensional equations. The reference measurements are:

Length - d

Velocity - U

Time - d^2/ν

Temperature - $qd^2/2\kappa Gr$.

Dimensionless variables are introduced where the Grashof number is $Gr = gaqd^5/2\nu^2\kappa$, this represents the temperature difference from heat transfer. The Prandtl number defines the physical property of a fluid and is equated $Pr = \frac{\nu}{\kappa}$. The Reynolds number is $Re = \frac{UL}{\nu}$, it characterises different flow regimes by how fast a fluid flows. It is proportional to the pressure gradient with respect to the non-dimensional parameters. Each of these variables are incorporated into equations (2.1)-(2.3), resulting in the non-dimensional forms of the equation. This is completed in Appendix A.

Non-Dimensional General Momentum Equation

$$\frac{\partial \mathbf{u}}{\partial t} + (\mathbf{u} \cdot \nabla)\mathbf{u} = -2Re + g\gamma T + \nabla^2 \mathbf{u}, \tag{2.8}$$

Non-Dimensional General Temperature equation

$$\frac{\partial T}{\partial t} + (\mathbf{u} \cdot \nabla)T = Pr^{-1}\left(\nabla^2 T + 2Gr\right). \tag{2.9}$$

Non-Dimensional Incompressibility condition

$$\nabla \cdot \mathbf{u} = 0\,. \tag{2.10}$$

Chapter 3

Formulating the problem

This chapter will focus on mathematically defining the problem and will determine the specific Navier Stokes equations with respect to the defined model. A description of the methods chosen to analyse the model problem will then be discussed.

3.1 Model Description

This dissertation considers an internally heated fluid bounded between two parallel plates and inclined at an angle χ, with an upper isothermal boundary and a lower adiabatic boundary. The Cartesian coordinate system is centred in the mid-plane of the layer, shown in Figure 3.1.

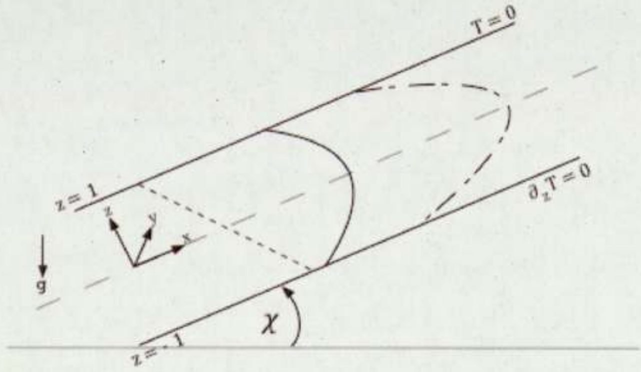

Figure 3.1: Geometric configuration of the model. The dash-dotted curve ($T_0(z) = Gr(-z^2 - 2z + 3)$) and the dashed line ($\partial_z T_0(z) = -(1 + z)$) indicate the trend in the basic temperature profile and its derivative over the layer depth. The solid curve illustrates the basic velocity profile. The temperature source originating internally. The whole channel is inclined at an angle χ degrees.

Following the work of (Nagata and Generalis, 2002) and (Generalis and Nagata, 2003), our interest is in the study of the flow when the channel is inclined. The buoyancy force acting on the system is denoted $g(\hat{\mathbf{k}}\cos\chi + \hat{\mathbf{i}}\sin\chi)$ where $\hat{\mathbf{i}}, \hat{\mathbf{j}}, \hat{\mathbf{k}}$ are the unit vectors that correspond to the x, y, z cartesian coordinates shown in Figure 3.1. This force is determined from the decomposition of the coordinate system. Accounting for this buoyancy term results in updating the non-dimensional Navier Stokes Equation (2.8), such that:

$$\frac{\partial \mathbf{u}}{\partial t} + (\mathbf{u}\cdot\nabla)\mathbf{u} = -2Re + g(\hat{\mathbf{k}}\cos\chi + \hat{\mathbf{i}}\sin\chi)T + \nabla^2\mathbf{u}, \tag{3.1}$$

$$\frac{\partial T}{\partial t} + \mathbf{u}\cdot\nabla T = Pr^{-1}\left(\nabla^2 T + 2Gr\right), \tag{3.2}$$

$$\nabla\cdot\mathbf{u} = 0. \tag{3.3}$$

We further constrain the problem modelled by defining conditions that correspond to the isothermal and adiabatic behaviour found at the boundaries.

Boundary Conditions:

$$T(z=1) = 0, \tag{3.4a}$$

$$\partial_z T(z=-1) = 0, \tag{3.4b}$$

$$u(z=\pm 1) = 0. \tag{3.4c}$$

The basic flow (U_0) and basic temperature (T_0) can be found by solving equations (3.1) and (3.2) respectively. To calculate the basic solutions of these equations, we assume the pressure gradient to constant, and the flow is assumed to be laminar.

3.1.1 Basic Temperature Solutions

The basic temperature equation is derived first as this temperature term is present in the velocity equation. Using equation (3.2) as a starting point, the convective term $[(\mathbf{u}\cdot\nabla)\,T]$ is neglected, this is because we are assuming the flow to be laminar. When determining the basic temperature we assume the flow is steady, therefore the time derivative $\left[\frac{\partial T}{\partial t}\right]$ is neglected also. By applying the boundary conditions a solution can be found.

Assume $T_0 \equiv T_0(z)$

$$\begin{aligned} \frac{1}{Pr}(\nabla^2 T_0 + 2Gr) &= 0, \\ \times Pr &\downarrow \times Pr \\ \nabla^2 T_0 + 2Gr &= 0. \end{aligned}$$

We can expand $\nabla^2 T_0$ such that:

$$\begin{aligned} \nabla^2 T_0 &= \left(\frac{\partial^2}{\partial x^2} + \frac{\partial^2}{\partial y^2} + \frac{\partial^2}{\partial z^2}\right) T_0(z), \\ &= \frac{\partial^2}{\partial z^2} T_0(z), \\ &= T_0''(z), \end{aligned}$$

Therefore we can write,

$$T_0''(z) + 2Gr = 0\,.$$

Now integrate $\int T_0''(z) + 2Gr\, dz$:

$$T_0'(z) = -2Gr[z] + A.$$

By substituting boundary condition (3.4b) into the above solution we achieve $A = -2Gr$. Integrate a second time $\int T_0'(z)\, dz = \int -2Gr[z] - 2Gr\, dz$:

$$T_0(z) = -Gr[z^2] - 2Gr[z] + B.$$

Substitute boundary condition (3.4a) into this second solution to solve for the unknown constant $B = 3Gr$. Once simplified the basic temperature equation can be defined as follows.

$$T_0(z) = Gr(-z^2 - 2z + 3). \tag{3.5}$$

3.1.2 Basic Velocity Solutions

Once the basic temperature is defined, an expression for the basic flow can be derived. Starting with equation (3.1) we can solve for the basic solutions after we simplify the equation. As stated we are looking at flow in a steady, laminar state, therefore the acceleration term $\left[\frac{\partial \mathbf{u}}{\partial t}\right]$, the convective terms$[(\mathbf{u} \cdot \nabla)\,\mathbf{u}]$ are neglected. The pressure gradient as previously explained is proportional to the Reynolds number $[-2Re]$, this is also equated to zero which results in:

$$\nabla^2 \mathbf{u_0} + g(\hat{\mathbf{k}} \cos \chi + \hat{\mathbf{i}} \sin \chi) T_0 = 0.$$

We can re-write the above equation in terms of its components.

$$\begin{aligned}
\nabla^2 \langle u_0(z), 0, 0 \rangle + g(\hat{\mathbf{k}} \cos \chi + \hat{\mathbf{i}} \sin \chi) T_0 &= 0, \\
&\downarrow \\
\nabla^2 u_0(z) + g(\sin \chi) T_0 &= 0.
\end{aligned}$$

Assume $u_0(z) \equiv U_0$. Next to simplify, let $-g(\sin \chi) = Q$ such that $\nabla^2 u_0 - QT_0 = 0$. This results in the following second order differential equation:

$$\frac{\partial^2}{\partial z^2} U_0 = U_0'' = QT_0,$$

now substitute the basic temperature solution $T_0(z)$ from equation (3.5) and integrate to achieve:

$$U_0' = QGr\left(\frac{-z^3}{3} - z^2 + 3z\right) + A.$$

Integrate a second time to get an expression for U_0 alone:

$$U_0 = QGr\left(\frac{-z^4}{12} - \frac{z^3}{3} + \frac{3z^2}{2}\right) + Az + B.$$

Finally using the no-slip boundary condition (3.4c) and solving the defined equation, we can find the unknown constants $A = \frac{1}{3} QGr$ and $B = -\frac{17}{12} QGr$. Once simplified we can obtain the basic flow equation:

$$U_0(z) = \frac{g}{12}(Gr \sin(\chi))(z^4 + 4z^3 - 18z^2 - 4z + 17). \tag{3.6}$$

When numerically implementing these equations, the Reynolds number becomes one of the parameters that is varied. In order to include this in the calculations, we explicitly and independently solve the solution for the Reynolds number term.

$$\int\int -2Re\, \partial z = Re(1 - z^2)$$

Therefore the numerical calculation takes the basic velocity solution U_0 in the form:

$$U_0(z) = \frac{g}{12}(Gr \sin(\chi))(z^4 + 4z^3 - 18z^2 - 4z + 17) + Re(1 - z^2). \tag{3.7}$$

When finding the parameters that correspond to the described basic state, we simply use the parameter $Re = 0$, this is the case when the pressure is regarded as constant and therefore no pressure gradient. The extra Reynolds number term goes and we are left finding a solution to (3.6).

3.2 Poloidal and Toroidal Decomposition

In order to analyse the stability of our fluid, it is necessary to also look at the deviations from the basic flow. We can express the velocity vector $\mathbf{u}$ in terms of a basic flow $\mathbf{U_0}$ and a slight deviation $\hat{\mathbf{u}}$ in the following way:

$$\mathbf{u} = \mathbf{U_0} + \hat{\mathbf{u}}. \tag{3.8}$$

Similarly the temperature can be expressed explicitly as a sum of the basic temperature distribution T_0 and small deviations $\hat{\theta}$ such that:

$$T = T_0 + \hat{\theta}. \tag{3.9}$$

By substituting these expanded terms into equation (3.1) - (3.3), we can then subtract all terms that correspond to the basic flow/temperature equations. This results in the perturbed governing equations being expressed explicitly in terms of the basic flow and temperature and their deviations:

$$\frac{\partial \hat{\mathbf{u}}}{\partial t} + (\mathbf{u_0} \cdot \nabla)\hat{\mathbf{u}} + (\hat{\mathbf{u}} \cdot \nabla)\mathbf{u_0} + (\hat{\mathbf{u}} \cdot \nabla)\hat{\mathbf{u}} = -2Re + g(\hat{\mathbf{k}}\cos\chi + \hat{\mathbf{i}}\sin\chi)\hat{\theta} + \nabla^2\hat{\mathbf{u}}, \quad (3.10)$$

$$\frac{\partial \theta}{\partial t} + (\mathbf{u_0} \cdot \nabla)\hat{\theta} + (\hat{\mathbf{u}} \cdot \nabla)\hat{\theta} = Pr^{-1}(\nabla^2\hat{\theta} + 2Gr), \quad (3.11)$$

$$\nabla \cdot \hat{\mathbf{u}} = 0. \quad (3.12)$$

The velocity deviation $\hat{\mathbf{u}}$ introduced in equation (3.8) is of the form:

$$\hat{\mathbf{u}} = \bar{U}(z,t) + \tilde{u}\,. \quad (3.13)$$

The average part of the velocity deviation field in the x,y-directions is denoted $\bar{U}(z,t)$. This over-bar average is calculated by the function $\left(\left(\alpha\beta/4\pi^2\right)\int_0^{2\pi/\alpha}\int_0^{2\pi/\beta} dxdy\right)$ which is the average value integral of the velocity function over the 2D region $[\alpha,\beta]$ where $0 \leq y \leq 2\pi/\alpha$, and $0 \leq x \leq 2\pi/\beta$. The second part of the velocity deviation field $\tilde{u}$ accounts for the fluctuation incurred. This fluctuation $\tilde{u}$ can be expanded using poloidal and toroidal components where:

$$\tilde{u} = \boldsymbol{\delta}\phi + \boldsymbol{\epsilon}\psi = \nabla \times \nabla \times (\hat{\mathbf{k}}\phi) + \nabla \times (\hat{\mathbf{k}}\psi), \quad (3.14)$$

ϕ and ψ are the poloidal and toroidal components respectively (Clever, 1977). Following the work of (Chandrasekhar, 1981), the $\boldsymbol{\delta}, \boldsymbol{\epsilon}$ operators are introduced to represent the solenoidal field of the velocity field. These operators can explicitly be expressed as:

$$\delta_i = \lambda_j \partial_i \partial_j - \lambda_i \Delta\,, \quad (3.15)$$

$$\epsilon_i = \epsilon_{ijk}\lambda_k \partial_j\,, \quad (3.16)$$

each operator component can be found by summing $i,j,k = 1,2,3$ the full derivation is completed in Appendix B. The result of summing over each index implies $\boldsymbol{\delta} = (\partial_x\partial_z, \partial_y\partial_z, -\Delta_2)$ and $\boldsymbol{\epsilon} = (\partial_y, -\partial_x, 0)$. The benefit of applying these operators is that we can remove the pressure gradient allowing us to ultimately represent our equations as a linear system. Another benefit is that we can analyse the 2D and 3D perturbations separately. By performing this expansion, we can reduce the number of parameters in the system. We end up with three equations and three unknown parameters ϕ , ψ and $\hat{\theta}$. In Appendix C the $\boldsymbol{\delta}, \boldsymbol{\epsilon}$ operators are applied to the momentum equation (3.10). This yields two distinct equations dependent only on the complex scalar functions ϕ , ψ and $\hat{\theta}$.

$$\frac{\partial}{\partial t}\nabla^2\Delta_2\phi + \bar{U}\partial_x\nabla^2\Delta_2\phi - \partial_z^2\bar{U}\Delta_2\partial_x\phi + \boldsymbol{\delta}\cdot\{(\boldsymbol{\delta}\phi + \epsilon\psi)\cdot\nabla(\boldsymbol{\delta}\phi + \epsilon\psi)\}$$
$$= \nabla^4\Delta_2\phi + \sin\chi\partial_x\partial_z\hat{\theta} - \cos\chi\Delta_2\hat{\theta}\,, \quad (3.17)$$

$$\frac{\partial}{\partial t}\nabla^2\psi + \bar{U}\partial_x\Delta_2\psi - \partial_z\bar{U}\Delta_2\partial_y\psi + \boldsymbol{\epsilon}\cdot\{(\boldsymbol{\delta}\phi + \epsilon\psi)\cdot\nabla(\boldsymbol{\delta}\phi + \epsilon\psi)\}$$
$$= \nabla^2\Delta_2\psi + \sin\chi\partial_y\hat{\theta}\,. \quad (3.18)$$

The same methodology is applied to the temperature, where the $\hat{\theta}$ deviation in equation (3.9) can be represented as:

$$\hat{\theta} = \bar{T}(z,t) + \tilde{\theta}, \quad (3.19)$$

the average is again represented by the over bar. Substituting the above deviations for $\hat{\mathbf{u}}$ and $\hat{\theta}$ into equation (3.11) and removing the basic temperature components we can obtain the following form:

$$\frac{\partial\hat{\theta}}{\partial t} = -2Gr(\mathbf{r}\cdot\mathbf{k})\Delta_2\phi + \Delta_2\phi\partial_z\bar{T} - \bar{U}\partial_x\hat{\theta} - (\boldsymbol{\delta}\phi + \epsilon\psi)\cdot\hat{\theta} + Pr^{-1}\nabla^2\hat{\theta}\,. \quad (3.20)$$

Each of our equations (3.17), (3.18) and (4.3) are subject to homogeneous boundary conditions:

$$\phi = \partial\phi/\partial z = \bar{U} = \psi = \bar{T} = \theta = 0 \qquad \text{at } z = \pm 1.$$

Once we have obtained equations (3.17) - (4.3) we can implement these computationally to solve for our unknown scalar functions. These can be defined such that:

$$\phi(x,y,z) = \sum_{n=0}^{\infty}(1-z^2)^2 T_n(z)a_n\exp\{i(\alpha x + \beta y) + \sigma t\}\,, \quad (3.21)$$

$$\psi(x,y,z) = \sum_{n=0}^{\infty}(1-z^2)T_n(z)b_n \exp\{i(\alpha x + \beta y) + \sigma t\}\,, \tag{3.22}$$

$$T(x,y,z) = \sum_{n=0}^{\infty}(1-z^2)T_n(z)c_n \exp\{i(\alpha x + \beta y) + \sigma t\}\,, \tag{3.23}$$

where a_n, b_n, c_n are the unknown coefficients. $T_n(z)$ are the nth order Chebyshev polynomials. In order for the boundary conditions to be satisfied, we use relevant functions; $(1-z^2)^2$ and $(1-z^2)$ for each scalar equation. In the above expressions, α and β correspond to the wave numbers, and σ are the real or imaginary eigenvalues.

Chapter 4

Linear Stability Analysis

This chapter provides a stability analysis of the defined model. The boundary between laminar flow and convection is determined. An in depth explanation of the method used to conclude the linear analysis is provided.

By looking at the linear stability of the problem, we are able to determine the region of parameters where our flow moves from a laminar basic sate to a state of convection. In these convective regions it is expected that a number of coherent structures will arise. When solving these linear stability equations, we disregard the non-linear terms for this first stage of analysis. The following equations are implemented:

$$\frac{\partial}{\partial t}\nabla^2\Delta_2\phi + \bar{U}\partial_x\nabla^2\Delta_2\phi - \partial_z^2\bar{U}\Delta_2\partial_x\phi = \nabla^4\Delta_2\phi + \sin\chi\partial_x\partial_z\hat{\theta} - \cos\chi\Delta_2\hat{\theta}\,, \tag{4.1}$$

$$\frac{\partial}{\partial t}\nabla^2\psi + \bar{U}\partial_x\Delta_2\psi - \partial_z\bar{U}\Delta_2\partial_y\psi + \epsilon\cdot = \nabla^2\Delta_2\psi + \sin\chi\partial_y\hat{\theta}\,. \tag{4.2}$$

$$\frac{\partial\hat{\theta}}{\partial t} = -2Gr(\mathbf{r}\cdot\mathbf{k})\Delta_2\phi + \Delta_2\phi\partial_z\bar{T} - \bar{U}\partial_x\hat{\theta} + Pr^{-1}\nabla^2\hat{\theta}\,. \tag{4.3}$$

In order solve these equations we need to equate the unknown scalar variables ϕ, ψ and $\hat{\theta}$. To solve the system of differential equations for the unknown variables, the Chebyshev collocation method is used.

4.1 Chebyshev Collocation Method

The Chebyshev collocation method is a specific case of a spectral method that when summed to infinity will produce an exact solution to a partial differential equation. When approximating a higher order PDE we recognise the probable case that there are infinitely many solutions. By a concept called discretisation we can replace this PDE with a finite dimensional problem (Mohanty et al., 2007).

Chebyshev polynomials are used for the approximation as they are generally fast converging. Also they provide a good approximation at the boundaries of the configuration as this is where the collocation points are most dense. By manipulating the governing equations, we obtain a momentum differential equation (3.17) in terms of the poloidal variable ϕ that has many unknowns. To solve this problem, we use the collocation method to discretise the continuous sum that characterises our unknown ϕ component. This allows us to optimise a number of equations at equal increments between our boundaries using Chebyshev Polynomials that can be solved as a linear system of equations.

The first step is to define our collocation points:

$$z_j = \cos\left\{\frac{(2j+1)\pi}{2N}\right\} \qquad \text{where } z_j = 0, 2, ..., N\,.$$

By expressing equations (3.21) - (3.23) in terms of these collocation points Z_j and truncating the sum to N, we can obtain solutions to the corresponding unknown scalar values. For the momentum equation (3.17), we solve for ϕ:

$$\phi(x, y, z) = \sum_{n=0}^{N}(1 - z_j^2)^2 T_n(z_j) a_n \exp\{i(\alpha x + \beta y) + \sigma t\}\,. \tag{4.4}$$

Once we have $N + 1$ ϕ-equations we then substitute these into equation (3.17) to achieve a linear system of equations that can be solved using the following generalised eigenvalue problem:

$$A\mathrm{x} = \sigma B\mathrm{x}\,. \tag{4.5}$$

We solve this eigenvalue problem numerically. Eigenvalue analysis is performed in order to deduce specific characteristics of the flow. The unknown coefficients correspond to the x component of equation (4.5). A and B are 2(N+1)×2(N+1) complex matrices whose elements are determined from equation (3.17).

The aim is to pinpoint a critical Grashof number (Gr_c) through Newton Raphson iterative method. This critical value is found when the real eigenvalues are zero, $\sigma_r = 0$. It is at this point that the eigenvalue moves from an unstable state (positive value) to stable state (negative value) or vice versus. This transition occurs at some combination of the critical wave numbers α_c or β_c. By varying the wave numbers it is possible to produce a neutral curve using a Newton Raphson iterative method, which highlights the boundary between stable and unstable behaviour corresponding to the particular cases studied. By varying the control parameters, we can summaries the behaviour of the fluid flow in changing circumstances.

4.2 Linear Stability Results

The first case studied, was the effect of varying the wave vectors alone. The specific wave number values that correspond to the coherent structures found in the flow heat patterns can be calculated using the following relation:

$$\alpha_c = \sqrt{\alpha^2 + \beta^2} = 4\alpha^2 . \tag{4.6}$$

The critical wave vector (α_c) for this particular system can be equated to 1.315 in accordance with (Tveitereid and Palm, 1976), (Glover et al., 2013). Using the above relationship and the critical wave number the following values are found for each structural type that can be expected.

Figure 4.1 shows the linear neutral curves for the varying wave numbers for Air ($Pr = 0.705$), Mercury ($Pr = 0.025$) and Water ($Pr = 7$) when in their basic state which occurs when Reynolds number = 0. The following Gr_c results were obtained for the horizontal orientation of the system, Air (3932.3), Mercury (110891.0) and Water (396.0).

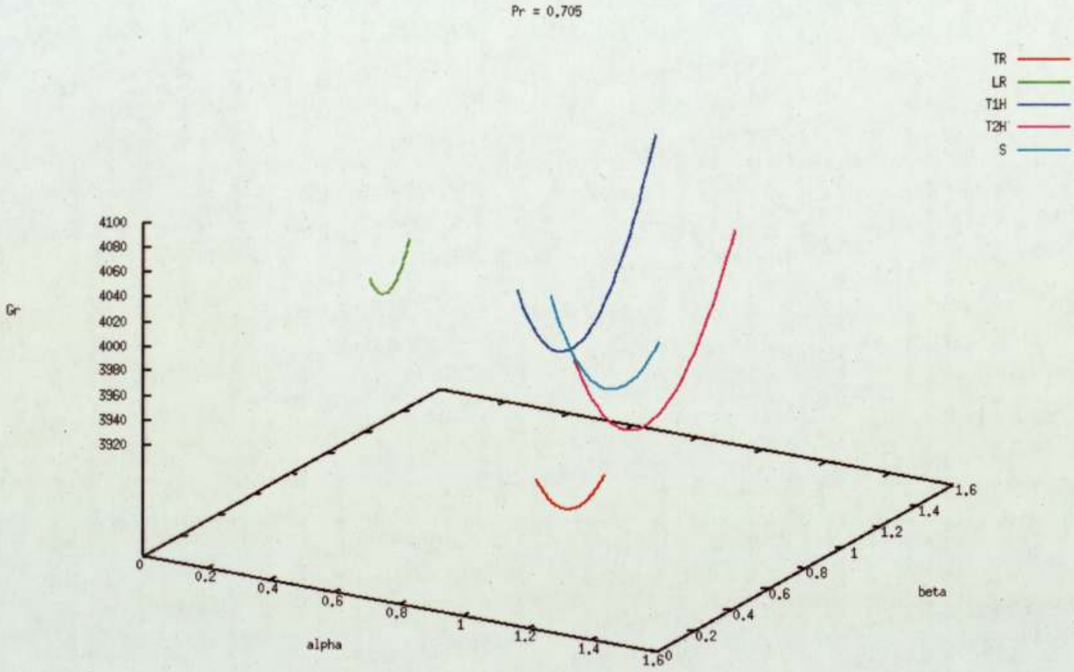

(a) Linear neutral curves for Air ($Pr = 0.705$)

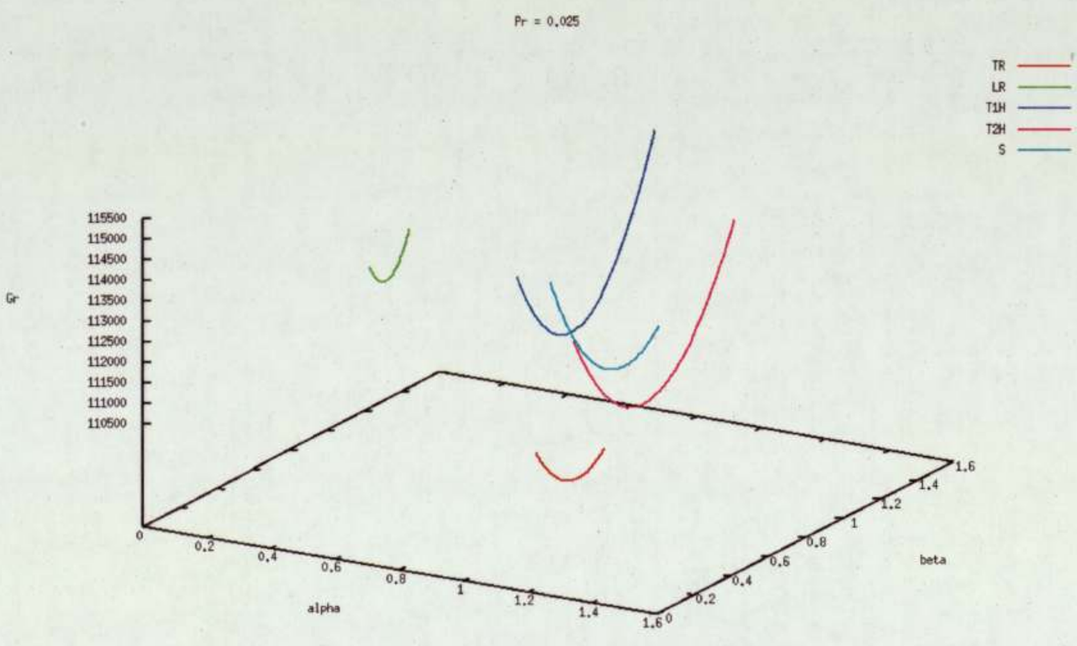

(b) Linear neutral curves for Mercury ($Pr = 0.025$)

Table 4.1: Table of structure types found with corresponding critical wave numbers.

	α_c	β_c
Transverse roll	1.315	0
Longitudinal roll	0	1.315
Type 1 Hexagon	0.658	1.139
Type 2 hexagon	1.139	0.658
Square	0.930	0.930

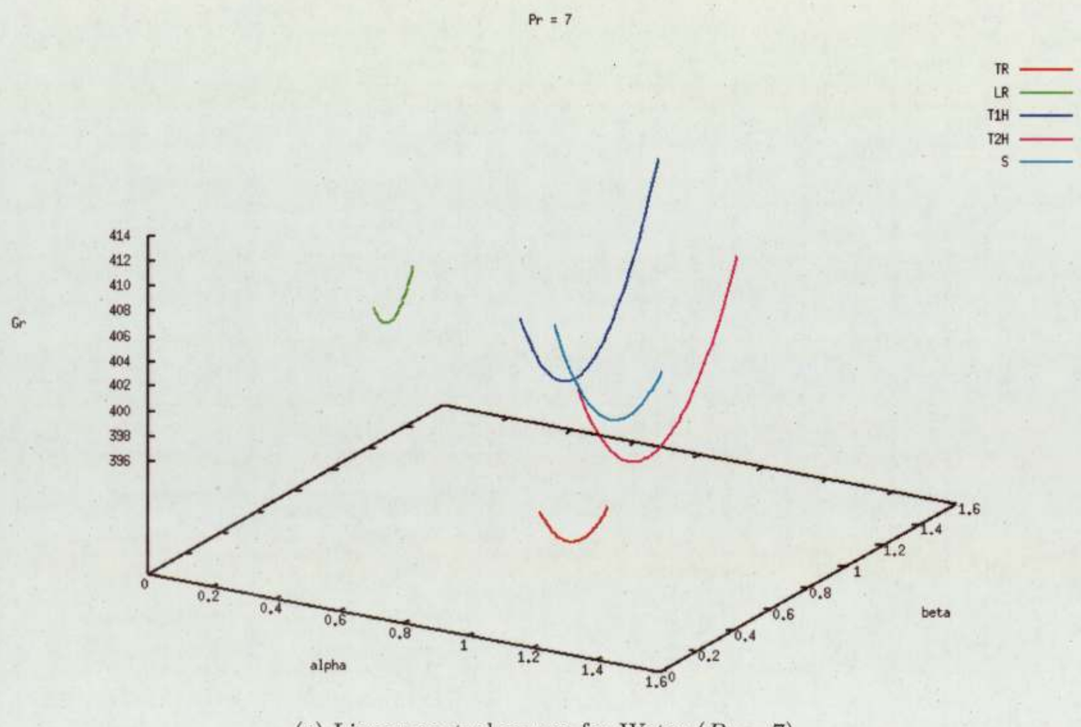

(c) Linear neutral curves for Water ($Pr = 7$)

Figure 4.1: The linear neutral curves for different structures with respect to the different fluid material when Reynolds number = 0.

For every case, the structures are reflected in the (α, β) direction and are perfectly symmetrical. This is due to the opposite orientation of transverse/longitudinal structures, as shown in Table 4.1. Following this analysis, we look at the effect of varying the Reynolds number. When in a basic state (Re = 0) it means there is no added pressure gradient in the stream-wise direction. However, by increasing this value we enforce a difference the flow regime such that the flow moves faster. We can deduce the effect this has on the critical Grashof number (Gr_c) and therefore the stability regions. We look solely at the effect the varying parameters have on the Grashof number because at higher Grashof numbers, the boundary layer is turbulent; at lower Grashof numbers, the boundary layer is laminar. We are looking at the first transition from a laminar flow to turbulent hence the region where this may occur.

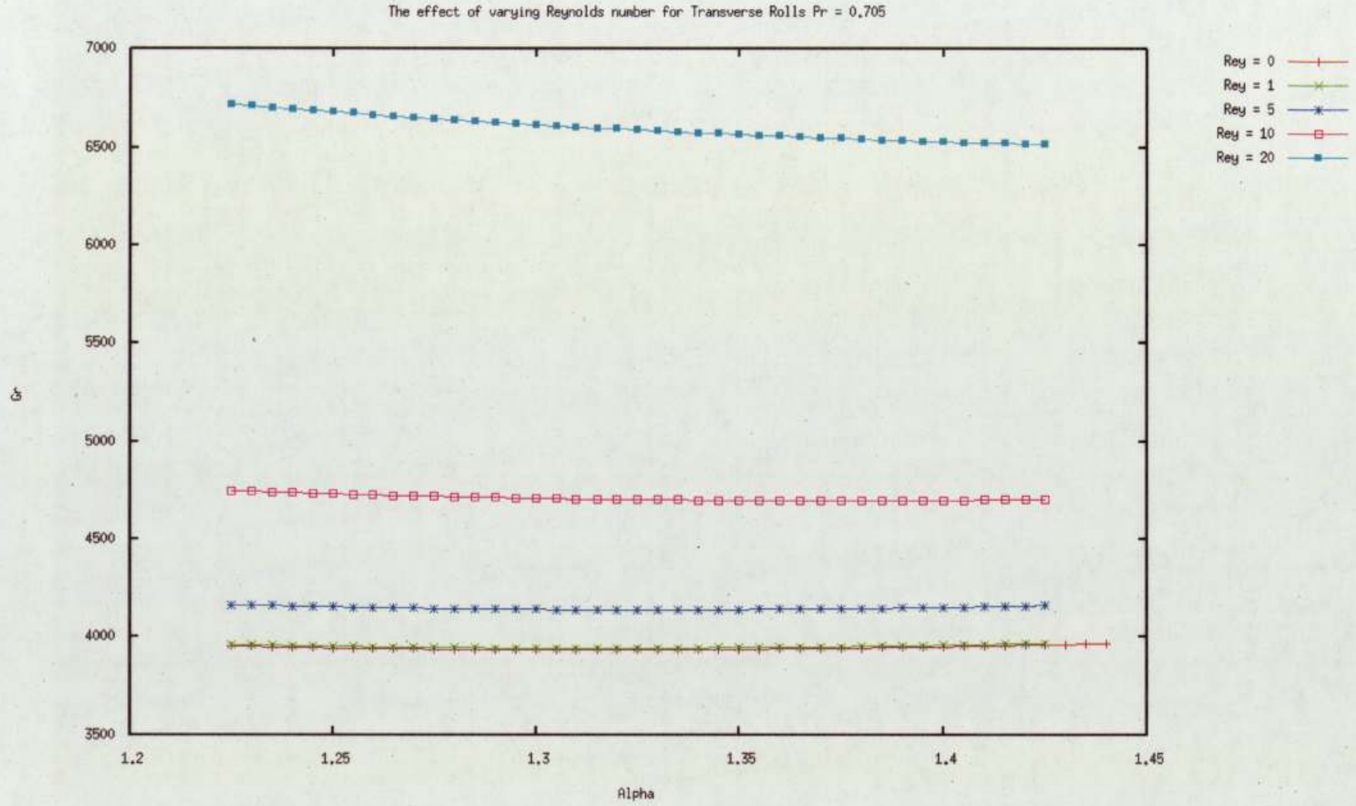

Figure 4.2: The effect of varying the Reynolds number for transverse rolls Pr = 0.705

The effect of increasing the Reynolds number has been demonstrated in Figure 4.2 for a transverse roll type structure with Pr = 0.705. We can see that as the Reynolds number is increased and consequently a larger pressure gradient is added, that the critical Grashof increases. Below the neutral curve is the stability region whereas above the curve is unstable region for each of the different Reynolds numbers. By comparing the critical Grashof values we can see that increasing the Reynolds number, increases the Grashof number, therefore a greater region where the fluid is stable. This result is consistent when varying the Reynolds number between 0 and 100 for Air, Mercury and Water for all structures.

A second case studied is where the angle of the channel in increased. As shown in Figure 3.1 we are particularly interested in seeing the effect of changing χ (in degrees) will have on the stability of the fluid. In order to see the effect of this, we plot the linear results when the angle is increasing in increments of 0.005, this is derived at the critical wave vector (α_c, β_c). The results vary depending on the type of structure being looked at, therefore an analysis for each structure will be done individually.

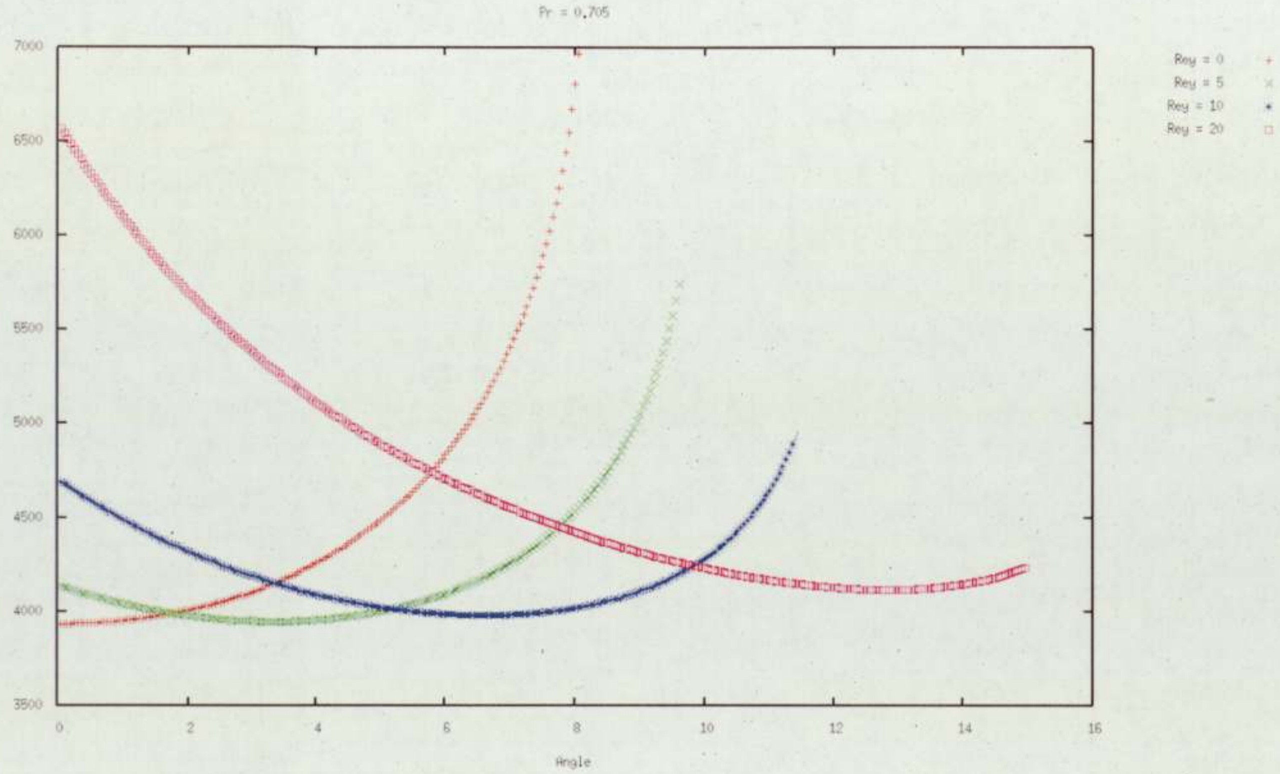

Figure 4.3: Transverse roll varying the angle and Reynolds number.

We begin with transverse rolls. Figure 4.3 shows the effect of increasing the angle and Reynolds number on the critical Grashof number. The results seem to suggest that at the purely basic state ($Re = 0$), the increased angle vastly increases the critical Grashof number value over a very small inclination. Therefore, as our channel moves from the horizontal orientation by the small angle indicated, our fluid becomes more stable. However as the Reynolds number increases also, we see that a new critical Grashof value occurs at varying increasing angles for each case. As the Reynolds number increases, the Grashof number falls further away from its critical value when horizontal, looking at the case where $Re = 20$ in Figure 4.3 we can see that as the inclination increases further ($> Re = 20$), the Grashof number never exceeds the Grashof value when horizontal. So for higher Reynolds numbers the fluid becomes unstable at much lower range of Grashof numbers, as the orientation of the channel moves from horizontal to vertical.

The next structure looked at is the longitudinal roll. Figure 4.4 shows very different results in comparison to Figure 4.3, it shows that the angle of inclination needs to significantly increased for it to have an effect on the stability. Only a small effect will take place where the Grashof number will rise. When the angle exceeds 50° the effect becomes more noticeable, with Gr increasing asymptotically as we approach the vertical orientation. This result is the same regardless of the Reynolds number when a Reynolds number between $0 - 100$ is applied. We conclude that for the longitudinal rolls, the stability changes are only dependent on the angle.

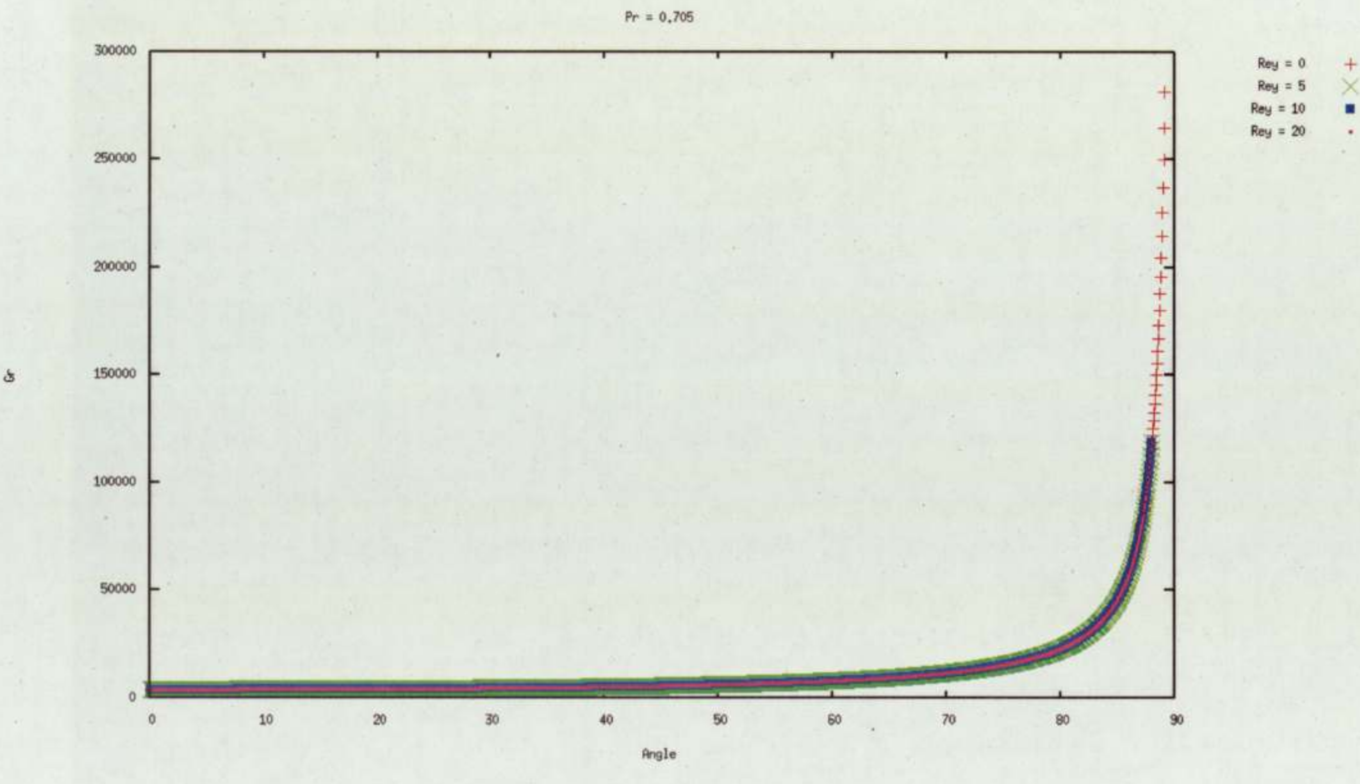

Figure 4.4: Longitudinal roll varying the angle and Reynolds number.

The major differences between Figure 4.3 and Figure 4.4 is a result of the structure orientation. For the transverse case the effect of the Reynolds number pushes the flow in across the roll structure causing differences. Whereas for the longitudinal case the added pressure gradient pushes the flow along the roll structure, hence the little disturbance regardless of the Reynolds number.

Following this we next analyse the type 1 hexagonal structures. The result of varying the angle and Reynolds number on the critical Grashof value for these structures are very

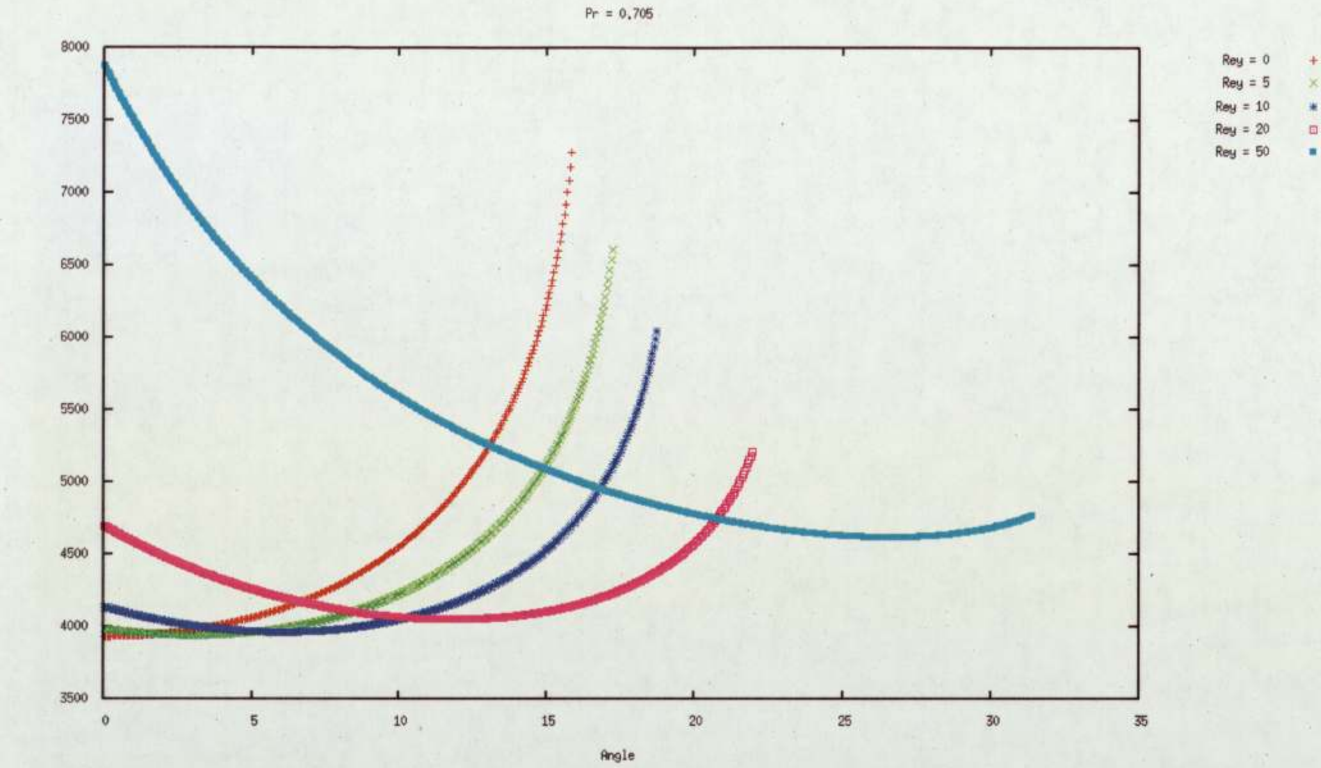

Figure 4.5: Type 1 hexagon varying the angle and Reynolds number.

similar to the transverse rolls (from Figure 4.3). A small increase in angle increases the critical Grashof number value. Although as the Reynolds number is increased simultaneously the Grashof value decreases and so becomes unstable at this lower value, shown in Figure 4.5. The Reynolds number needs to be larger for this effect to be seen, $Re = 50$ in Figure 4.5 exhibits a similar pattern to $Re = 20$ from the transverse roll type structure.

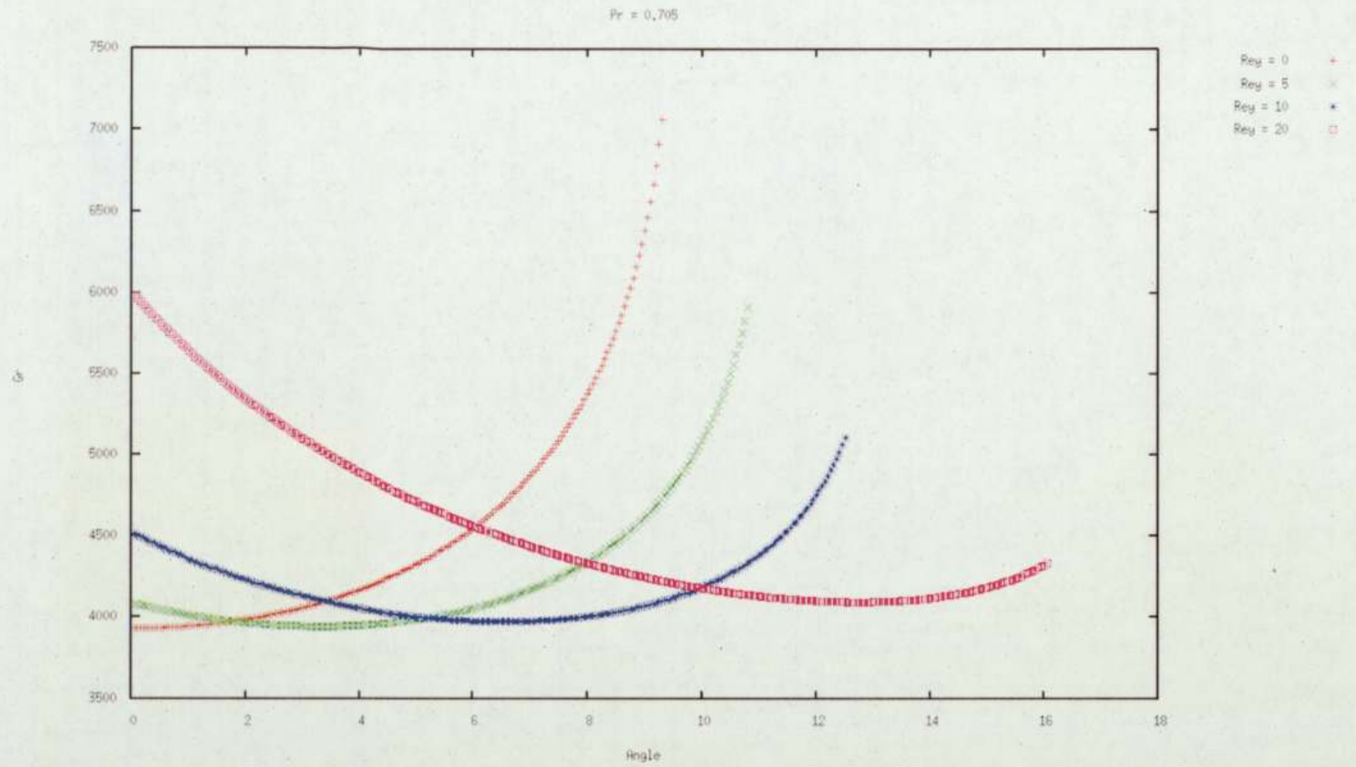

Figure 4.6: Type 2 hexagon varying the angle and Reynolds number.

The fourth structure we analyse is the type 2 hexagons. In Figure 4.6 we can see that the structure demonstrates similar behaviour to the transverse rolls and type 1 hexagons. More like the rolls it takes a lower value of the Reynolds number for the Grashof number to show decreasing behaviour and therefore lowering the range of Grashof number for stable behaviour. The difference between the type 1 and 2 hexagons is their wavelength orientation, they are perpendicular.

The final structural type to consider is the square structure in Figure 4.7. The squares behave consistently with Figures 4.3, 4.5 and 4.6. Similar to the type 1 hexagons a higher Reynolds number of 50 is used to show the full effect that increasing the angle will have on the basic state when a Reynolds number is implied.

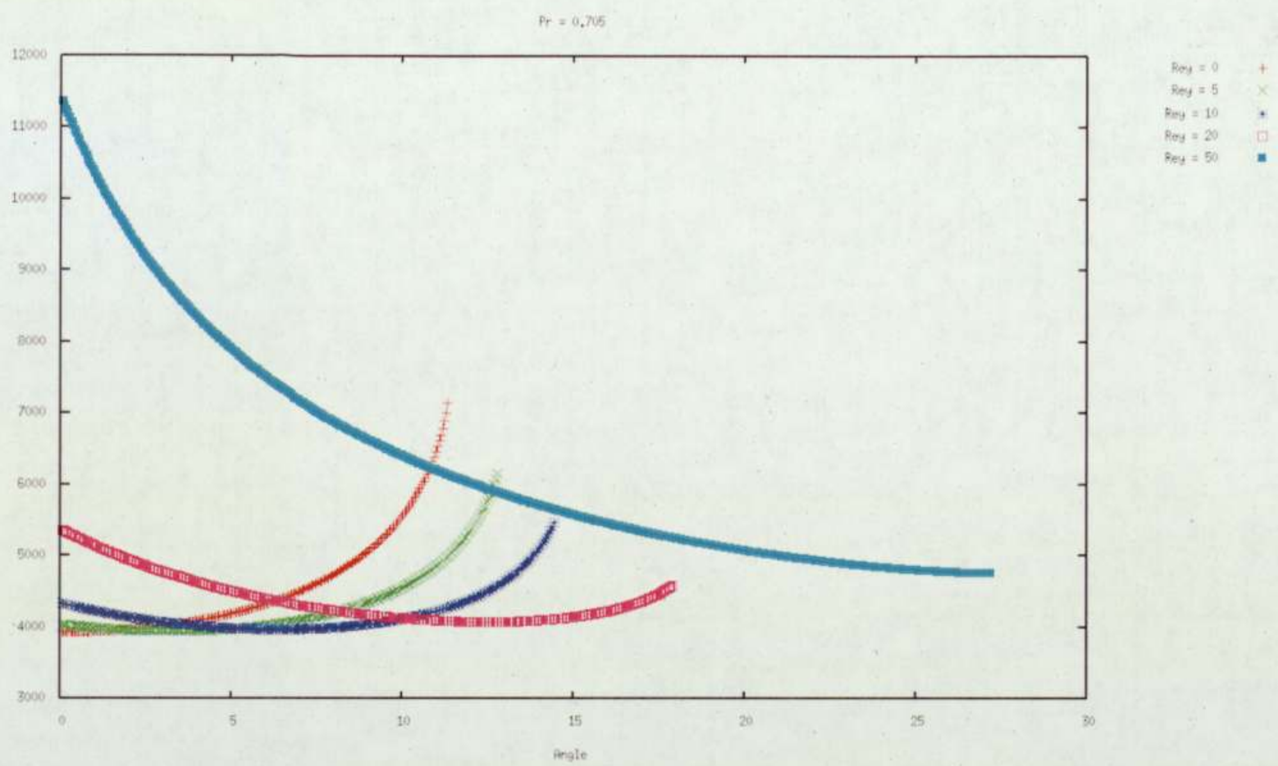

Figure 4.7: Square structure varying the angle and Reynolds number.

Generally these results are consistent for all structures with the exception of longitudinal rolls. We can conclude that with the exception of the longitudinal rolls, increasing the angle of inclination of the channel increases the critical Grashof number value therefore meaning the fluid is in a laminar, stable state more for very small Reynolds numbers. When the Reynolds number increases to a larger values this behaviour changes and acts in an opposite manner. The range of Reynolds number where this change in behaviour occurs is around $Re = 15$. Further numerical experiments can be used to pinpoint the exact value, however this isn't necessary for this study.

	Rey №	*Gr №*
Transverse Rolls	**0**	**3932.349**
	1	3939.590
	5	4132.190
	10	4691.722
	20	6570.713
Longitudinal Rolls	0	3932.349
	1	3932.349
	5	3932.349
	10	3932.349
	20	3932.349
Type 1 Hexagon	**0**	**3932.349**
	1	3934.129
	5	3983.263
	10	4135.154
	20	4697.782
	50	7872.634
Type 2 Hexagon	**0**	**3932.349**
	1	3945.218
	5	4083.180
	10	4513.533
	20	5982.88
Squares	**0**	**3932.349**
	1	3935.950
	5	4033.544
	10	4328.418
	20	5366.173
	50	11361.293

(a) $\chi = 0$

	Rey №	*Gr №*
Transverse Rolls	0	-
	1	-
	5	5657.643
	10	4283.126
	20	**4229.091**
Longitudinal Rolls	0	3992.966
	1	3992.966
	5	3992.966
	10	3992.966
	20	3992.966
Type 1 Hexagon	0	4549.194
	1	4469.993
	5	4220.383
	10	**4046.874**
	20	4065.800
	50	5589.51
Type 2 Hexagon	0	-
	1	-
	5	5088.518
	10	4186.839
	20	**4181.482**
Squares	0	5540.944
	1	5277.570
	5	4543.762
	10	**4110.253**
	20	4127.676
	50	6408.787

(b) $\chi = 10$

Table 4.2: Analysis of the Gr values corresponding to different structures when Reynolds number is increased for a selection of small values. These tables show (in bold) the lowest Gr and Reynolds value for $\mathrm{Pr} = 0.705$ when $\chi = 0$ and $\chi = 10$ respectively.

There are a number of trends in Table 4.2 worth noting. Firstly we can see that for all the longitudinal roll cases included, the Grashof value remains constant regardless of the angle or Reynolds number. For all elements labelled '-' the neutral curve was not found at the particular angle for the respective Reynolds value. When $\chi = 0$ the lowest Grashof number is in fact our critical Grashof number at Reynolds $= 0$. However we can see how increasing the Reynolds number effects the Gr value for this horizontal orientation. When $\chi = 10$, the critical Grashof number appears to be influenced by the Reynolds number, the Gr_c has a higher value suggesting as the Reynolds number increases the flow becomes less stable.

Chapter 5

Non-Linear Stability Analysis

This chapter describes the motivation of the non-linear analysis with instruction on how we produced our results. The results of our analysis are presented with concluding remarks on what has been found in the research to date.

5.1 Non-Linear Solutions

We adopt the same methodology used in the linear stability analysis, to determine the stability of the strongly non-linear states found in the secondary flow. We look at the unstable region of the fluid just above the neutral curve boundary found in the previous chapter, and perform the numerical non-linear analysis. Firstly we need to determine the non-linear state parameter space. We do this by referring back to our Navier Stokes equations (3.1) - (3.3). For the Non-Linear solutions we neglect the acceleration term $[\frac{\partial \mathbf{u}}{\partial t}]$ as we are looking at a steady flow, we include all other terms. Then using the poloidal/toroidal decomposition we expand the Navier Stokes equations in terms of the basic flow/ temperature and the corresponding perturbations. Following the same method as described in Chapter 3.2, the following equations are numerically solved:

$$\bar{U}\partial_x\nabla^2\Delta_2\phi - \partial_z^2\bar{U}\Delta_2\partial_x\phi + \boldsymbol{\delta}\cdot\{(\boldsymbol{\delta}\phi + \boldsymbol{\epsilon}\psi)\cdot\nabla(\boldsymbol{\delta}\phi + \boldsymbol{\epsilon}\psi)\}$$
$$= \nabla^4\Delta_2\phi + \sin\chi\partial_x\partial_z\hat{\theta} - \cos\chi\Delta_2\hat{\theta}\,, \quad (5.1)$$

$$\bar{U}\partial_x\Delta_2\psi \;-\; \partial_z\bar{U}\Delta_2\partial_y\psi \;+\; \epsilon\cdot\{(\delta\phi+\epsilon\psi)\cdot\nabla(\delta\phi+\epsilon\psi)\} \;=\; \nabla^2\Delta_2\psi \;+\; \sin\chi\partial_y\hat{\theta}\,. \quad (5.2)$$

$$2Gr(\mathbf{r}\cdot\mathbf{k})\Delta_2\phi = \Delta_2\phi\partial_z\bar{T} - \bar{U}\partial_x\hat{\theta} - (\delta\phi+\epsilon\psi)\cdot\hat{\theta} + Pr^{-1}\nabla^2\hat{\theta}\,. \quad (5.3)$$

In order to find a solution to the unknown scalar variables, we use equations (3.21) - (3.23) and again truncate our sum using the chebyshev collocation method. By solving the generalised eigenvalue problem, we identify the non-linear state parameters when $\sigma_r = 0$.

5.2 Non-linear Stability Analysis

For the non-linear stability analysis we use the solutions to equation (5.1), (5.2) and (5.3) and perform a linear stability test on these strongly non linear states. To test the stability of these states, we use Floquet Theory to include complex disturbances to the scalar derivation (Kuchment, 1982). These Complex disturbances are applied to ϕ, ψ and θ, which can be expressed fully as:

$$\tilde{\phi}(x,y,z) = \sum_{m=-\infty}^{\infty}\sum_{n=0}^{\infty}(1-z^2)^2T_n(z)\tilde{a}_{mn}\exp\{i(m\alpha+d)(x-ct)+iby+\sigma t\}\,, \quad (5.4)$$

$$\tilde{\psi}(x,y,z) = \sum_{m=-\infty}^{\infty}\sum_{n=0}^{\infty}(1-z^2)T_n(z)\tilde{b}_{mn}\exp\{i(m\alpha+d)(x-ct)+iby+\sigma t\}\,, \quad (5.5)$$

$$\tilde{\theta}(x,y,z) = \sum_{m=-\infty}^{\infty}\sum_{n=0}^{\infty}(1-z^2)T_n(z)\tilde{c}_{mn}\exp\{i(m\alpha+d)(x-ct)+iby+\sigma t\}\,. \quad (5.6)$$

Where $T_n(z)$ are the n-th order chebyshev polynomials, $\tilde{a}_{nm}, \tilde{b}_{nm}, \tilde{c}_{nm}$ are the unknown complex coefficients. d and b are the newly introduced complex disturbances, and c is the phase velocity. The homogeneous boundary conditions $\tilde{\phi} = \partial\tilde{\phi}/\partial z = \tilde{\psi} = 0$ at $z = \pm 1$ are satisfied for equations (5.1) - (5.3) and are accounted for in the functions $(1-z^2)^2$ and $(1-z^2)$ for the unknown $\tilde{\phi}, \tilde{\psi}$ and $\tilde{\theta}$.

To derive the disturbance field $(\tilde{\phi}, \tilde{\psi}, \tilde{\theta})$, we substitute $\phi + \tilde{\phi}$, $\psi + \tilde{\psi}$ and $\theta + \tilde{\theta}$ into equations (5.1) - (5.3). We numerically solve the updated equations again by means of a generalised eigenvalue problem:

$$A\tilde{x} = \sigma B\tilde{x}. \quad (5.7)$$

We solve this to find the real and imaginary eigenvalues for each perturbed flow state. A and B are 3(N+1)(2M+1) complex matrices that correspond to equations (5.1) - (5.3). It is worth noting that we make the assumption that no factors contribute to the mean flow or mean temperature such that $d^2 + b^2$ have non zero values. By solving the eigenvalue problem we can analyse the behaviour of the flow with respect to the eigenvalues. We expect for all $\sigma_r < 0$ the state to exhibit stable behaviour and therefore unstable for $\sigma_r > 0$, the real part of our eigenvalue determines the rate of damping in the case of negative values and amplification in the case of the positive values for the disturbances.

5.3 Non-linear Stability Results

To briefly recap, in the linear analysis, we look at the effect that changing the angle has on the critical Grashof number for different fluid materials. The boundaries between a stable laminar state and convection are identified at different wave numbers where we expect to find different structures. We find the non-linear state parameter space just above this boundary and trace the parameters with respect to the angle. In order to identify the the properties of the identified non-linear states, a further stability analysis is performed.

We add small perturbations to our configuration matrix and try to identify any 2D or 3D states at the specific wave numbers, angles and Prandtl. We can adjust these control parameters in any combination and so there may be more than one state at any wavenumber or angle. We do further linear analysis on the states to determine whether they are stable or unstable.

As an extension of the work done in the linear analysis we focus on the case where the $Re = 0$. This gives a completely isotropic convective flow, by inclining the channel we induce velocity vis the basic profile which introduces anisotropy. When analysing the results, firstly we look at how the poloidal $\phi : \ell_2$-norms differ depending on the structures and by changing the angle, where the heat applied is just above the criticality.

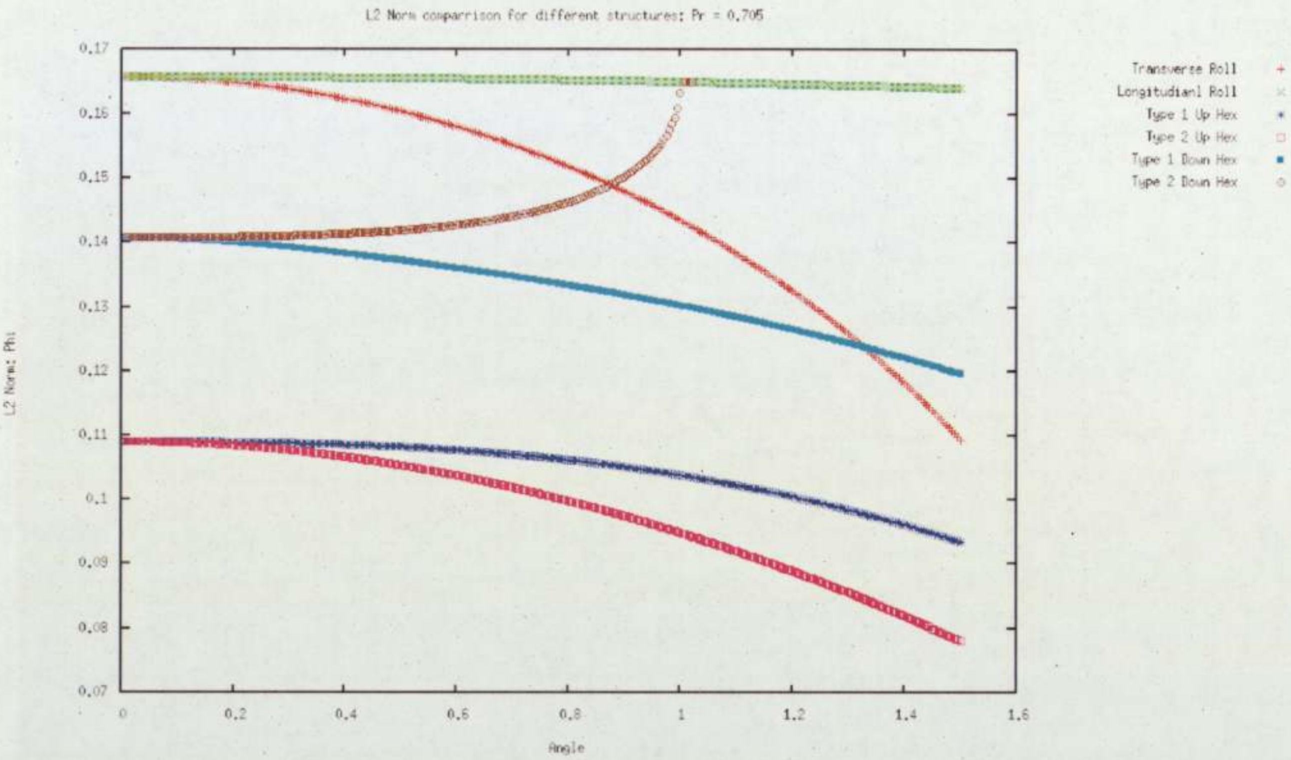

(a) $\phi : \ell_2$-norm for Air

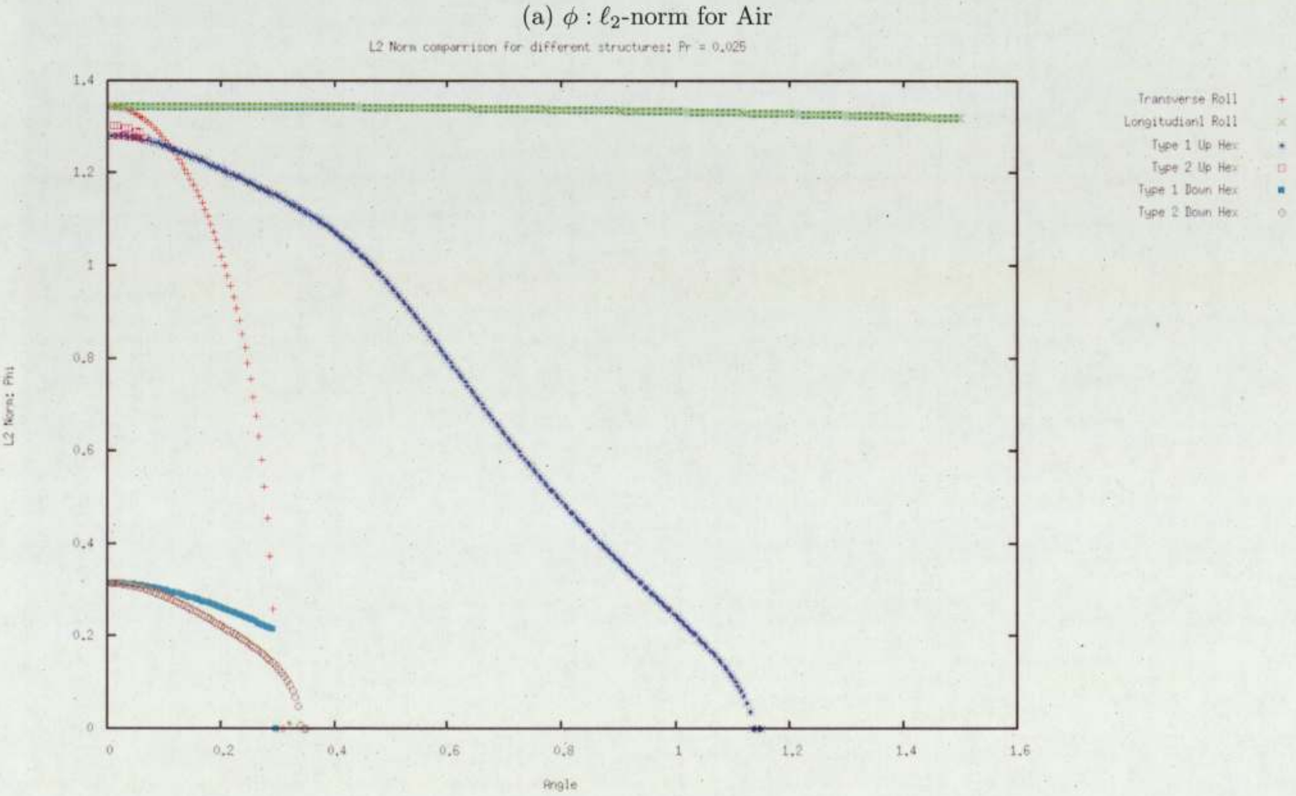

(b) $\phi : \ell_2$-norm for Mercury

Figure 5.1: The behaviour of the $\phi : \ell_2$-norms for two different Prandtl numbers when a small angle is applied.

There are clear major differences between Figures 5.1(a) and (b). By looking first at Figure 5.1(b), we can deduce from our results that for very small Prandtl number such as Mercury (Pr $=$ 0.025), all structures do not exist beyond the angle $\chi = 1.13$ with the exception of the longitudinal rolls. The longitudinal rolls appear to maintain their strength under this small angular difference. From this diagram the longitudinal rolls are most excited and could be the cause of maximum heat transfer, therefore suggesting the most economical way to transfer heat is via roll structures. The type 1 down hexagons appear to align with the transverse rolls around the angle $\chi \approx 0.3$.

Comparing this analysis with Figure 5.1(a) we can see similar behaviours. Most of the structures appear to decrease in value and so show tendencies to disappear over a larger increase in angle. In the case of Air(Pr $=$ 0.705) an interesting result is that the down type 2 hexagon appears to overcome the transverse roll to eventually completely align with the longitudinal rolls around the angle $\chi = 1$.

When looking at the the behaviour of the $\psi : \ell_2$-norms in Figure 5.2, we can see for the case of very small Prandtl number the only structure that exists beyond the boundary of $\chi \approx 1.4$ is the longitudinal rolls. For the case of Air, the result are not as conclusive. There is no ψ-norm for the transverse rolls due to their 2D structure. For the down hexagons in this small range of angle, the curve appears to be increasing in strength. However increasing the analysis to a larger range of angle could show this trend to curve and begin to decrease in the same manner as with the $\phi : \ell_2$-norms.

Analysis of the $\theta : \ell_2$-norms confirms our assumptions that longitudinal rolls appear to dominate the heat transfer for the two cases where we increase the angle of the channel for Air and Mercury when Re $= 0$. When looking at the Mercury case, the type one down hexagons and and transverse rolls align, this is due to the transverse rolls being a more stable structure and therefore the down hexagons loose their structure and so it is likely the numerical calculation tracked the rolls at this point. Further analysis at a greater range of angles can be done to determine the angular value where the structures decease for the case of Air, for Mercury this value is $\chi \approx 1.14$.

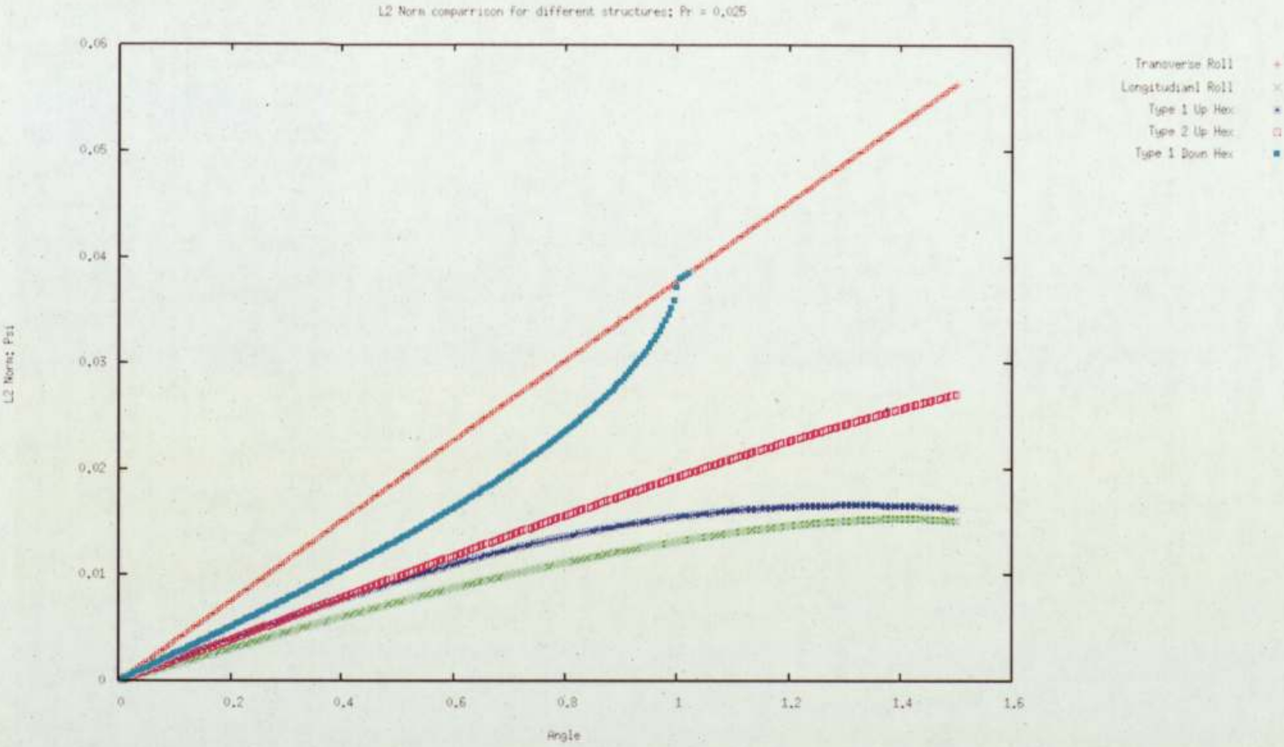

(a) $\psi : \ell_2$-norm for Air

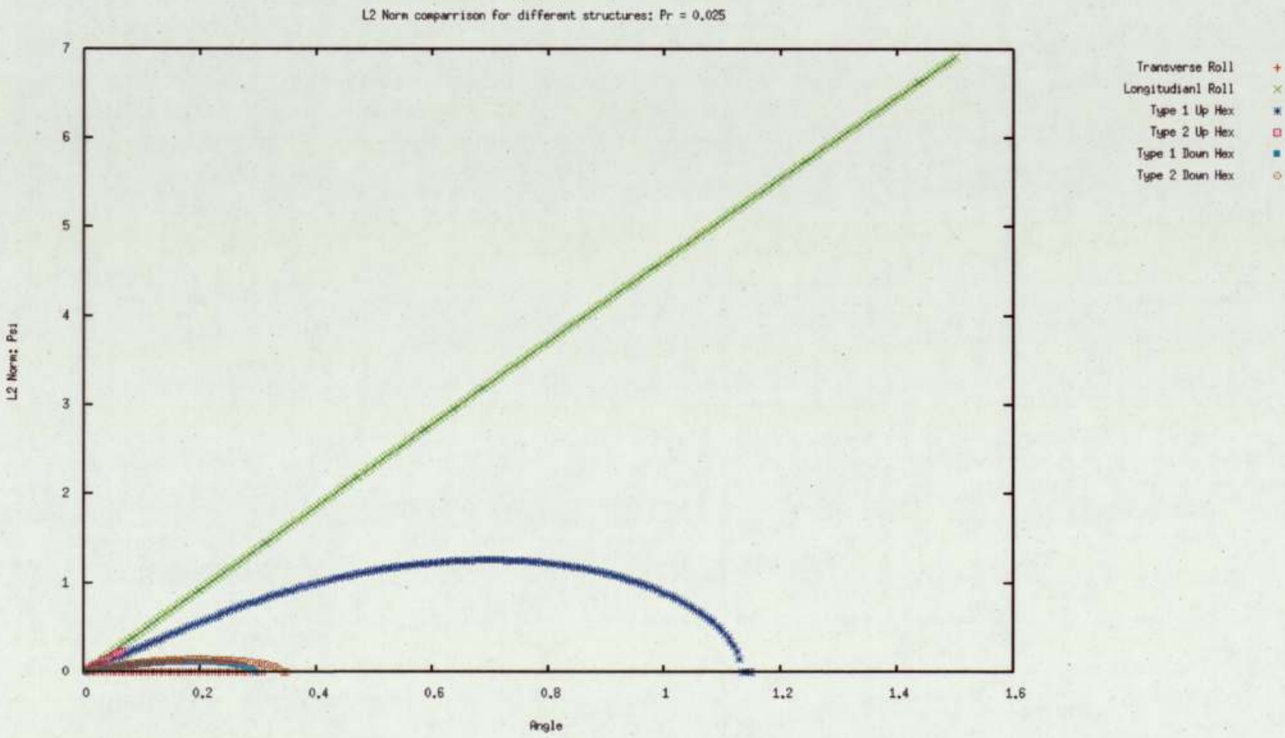

(b) $\psi : \ell_2$-norm for Mercury

Figure 5.2: The behaviour of the $\psi : \ell_2$-norms for two different Prandtl numbers when a small angle is applied.

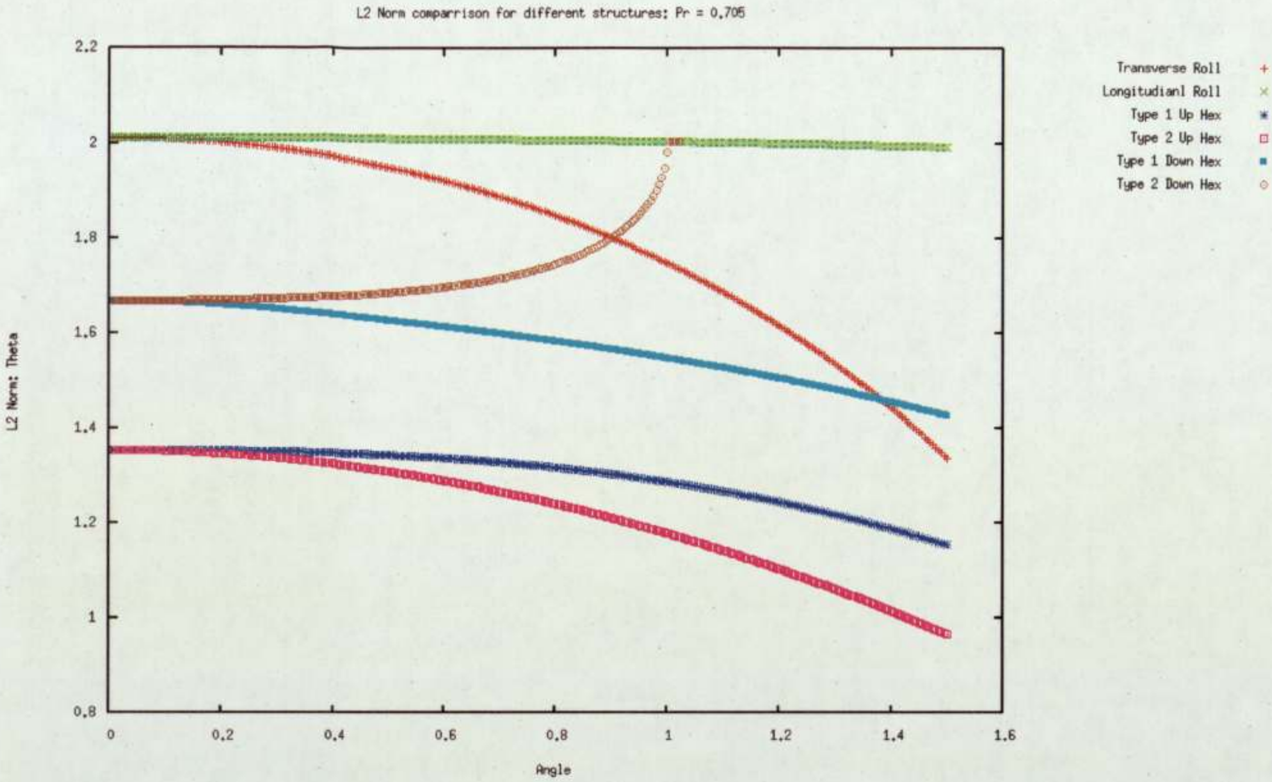

(a) $\theta : \ell_2$-norm for Air

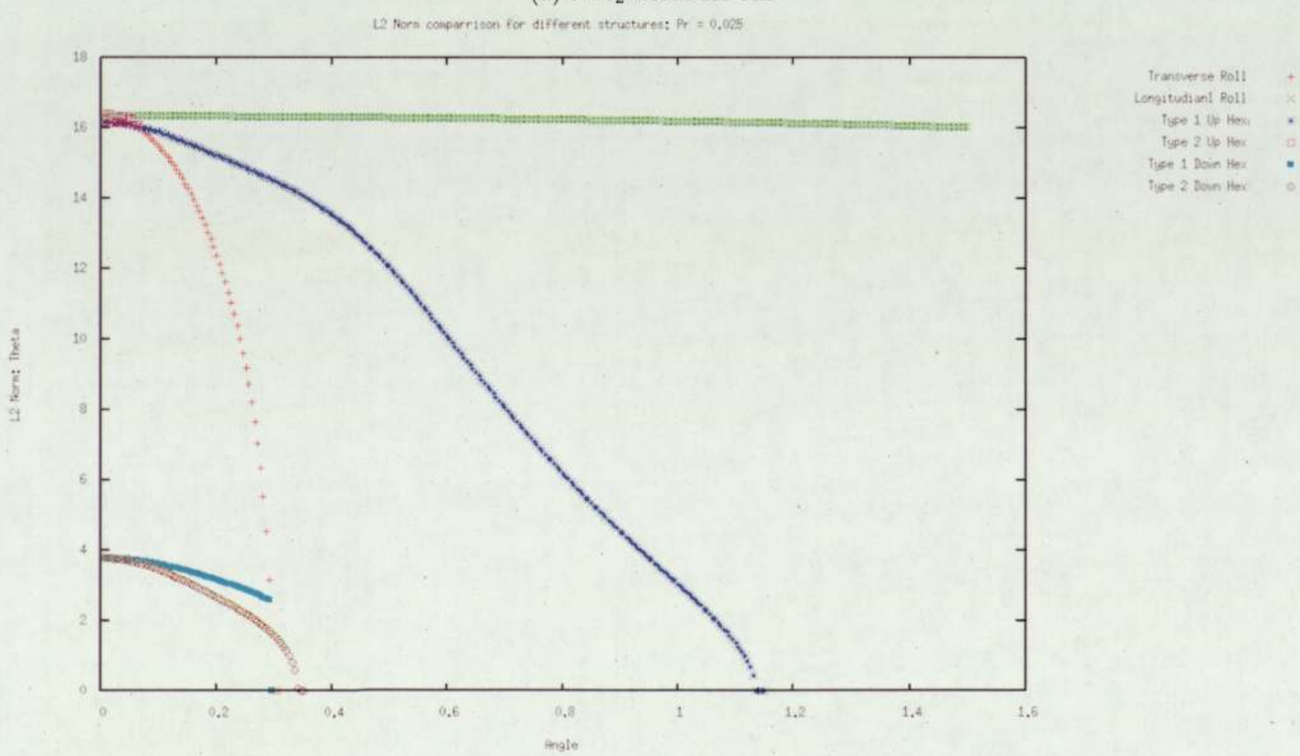

(b) $\theta : \ell_2$-norm for Mercury

Figure 5.3: The behaviour of the $\theta : \ell_2$-norms for two different Prandtl numbers when a small angle is applied.

Table 5.1: The changing values of the matrix size chosen for analysis and the ℓ_2 - norms found corresponding to the different coherent structures found where (α, β) are the respective wave numbers such that : Transverse roll (0,1.315); Longitudinal Roll (1.315,0); Type 1 Hex (0.66,1.14); Type 2 Hex (1.14,0.66). Values are consistent to the case where $\mathrm{Pr} = 0.705$, $\mathrm{Rey} = 0$, $\chi = 1^\circ$.

	L	M	N	$\phi : \ell_2$-norm	$\psi : \ell_2$-norm	$\theta : \ell_2$-norm
Transverse Roll	17	5	0	0.14354356	-	1.74952734
Longitudinal Roll	17	0	5	0.16500109	0.03778987	2.00516547
Type 1 Up Hex	21	10	6	0.10385051	0.01316288	1.28764875
Type 2 Up Hex	21	6	10	0.09487824	0.01550656	1.17936815
Type 1 Down Hex	21	10	6	0.13028698	0.01929889	1.54905022
Type 2 Down Hex	21	6	10	0.16339347	0.03715104	1.98286988

Table 5.2: The changing values of the matrix size chosen for analysis and the ℓ_2 - norms found corresponding to the different coherent structures found where (α, β) are the respective wave numbers such that : Transverse roll (0,1.315); Longitudinal Roll (1.315,0); Type 1 Hex (0.66,1.14); Type 2 Hex (1.14,0.66). Values are consistent to the case where $\mathrm{Pr} = 0.025$, $\mathrm{Rey} = 0$, $\chi = 1^\circ$.

	L	M	N	$\phi : \ell_2$-norm	$\psi : \ell_2$-norm	$\theta : \ell_2$-norm
Transverse Roll	21	16	0	-	-	-
Longitudinal Roll	21	0	16	1.33321132	4.62879339	16.20999646
Type 1 Up Hex	21	10	6	0.24388119	0.89027460	3.04306479
Type 2 Up Hex	21	6	10	-	-	-
Type 1 Down Hex	21	10	6	0.31471826	0.00003195	3.78666816
Type 2 Down Hex	21	6	10	-	-	-

We summarise the ℓ_2-norm values with details of the number of modes used in the calculations in Tables 5.1 and 5.2. For all zero values in the table, we do not numerically find a solution for the corresponding structure at the angle $\chi = 1^\circ$.

We want to explore the trends in stability for our non-linear results when a disturbance is added to our states. To deduce any information about the stability of the states we need to take a closer look at the eigenvalue components. There are specific trends that we are looking for with this eigenvalue analysis. When looking at the real eigenvalues σ_r we analyse whether our results are > 0. For all the cases where we do have a positive real eigenvalue the structures are unstable. Our main goal is to determine if these non-linear state parameters exhibit stable or unstable behaviour.

The imaginary eigenvalues σ_i are also analysed to determine the behaviour of the structures. For our analysis, if the imaginary eigenvalues show no significant trends, we assume the structures are stationary waves. If the two eigenvalues have the same magnitude but opposite sign, it suggests they are oscillating. Oscillatory waves are roll or knots states that oscillate with time. If one of the eigenvalues is constant and the second shows a significant declining trend, then it is assumed to be a travelling wave. Travelling waves are states that have a phase velocity, they move in space and time.

5.3.1 Stability Analysis Air (Pr = 0.705)

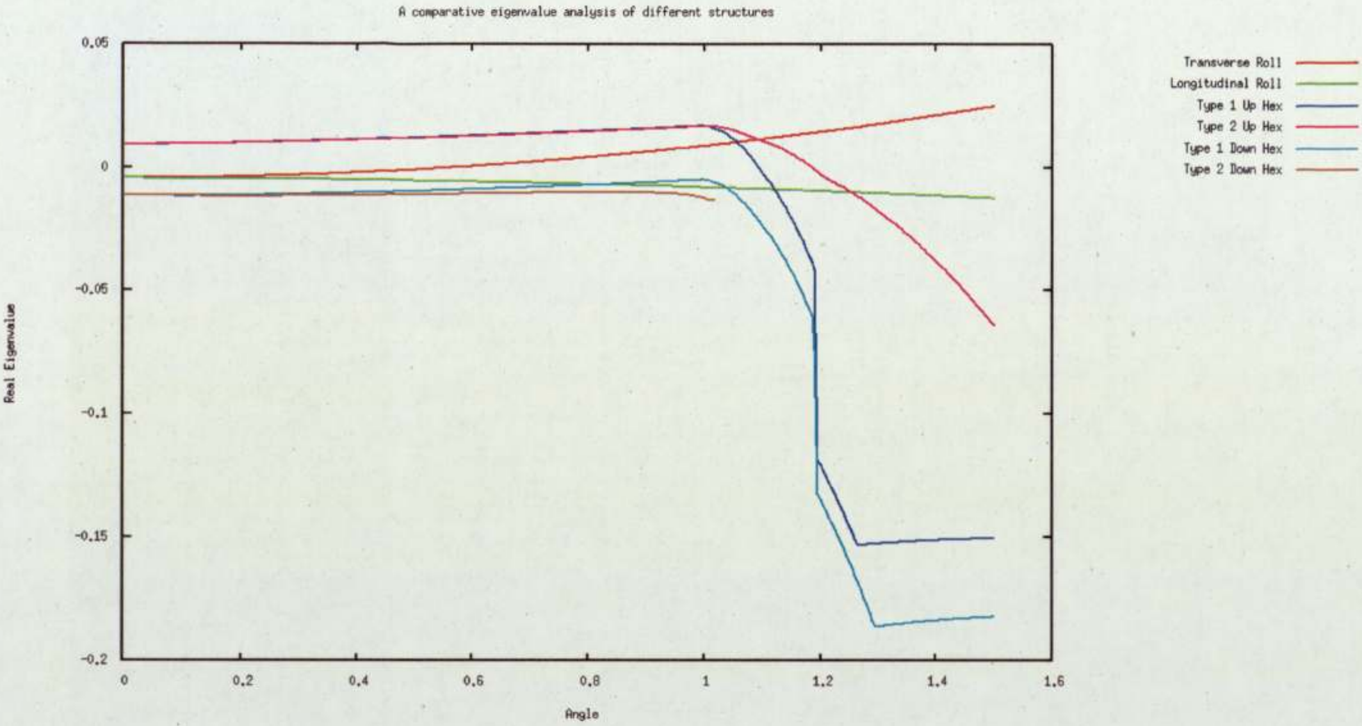

Figure 5.4: Real Eigenvalues against a small angle variation for Air (Pr = 0.705). For each structural type a disturbance (d, b) is applied such that: Transverse roll $(0, 1.315)$; Longitudinal roll $(1.315, 0)$; Type 1 Up/Down Hex $(1.14, 0.66)$; Type 2 Up/Down Hex (0.66,1.14).

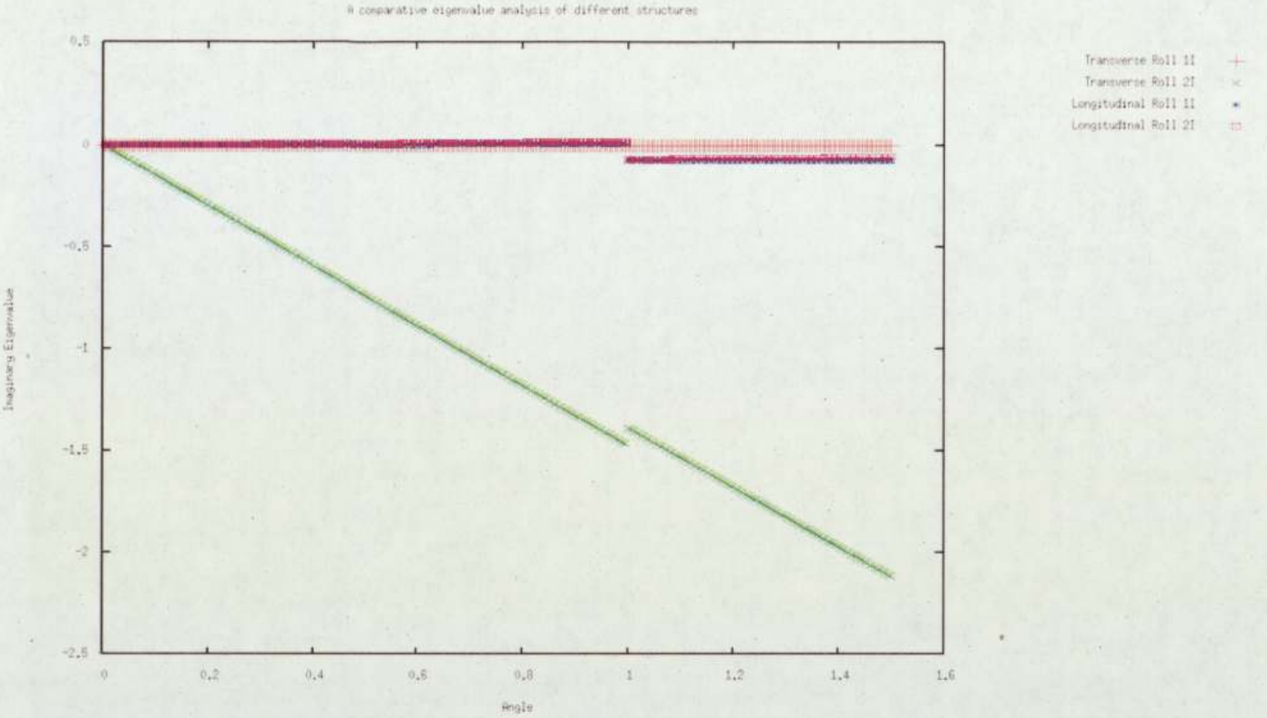

Figure 5.5: Imaginary Eigenvalues against a small angle variation for Air (Pr = 0.705). A disturbance (d, b) is applied to the structures such that: Transverse roll $(0, 1.315)$; Longitudinal roll $(1.315, 0)$.

Figure 5.4 shows that both the roll structures are stable at a horizontal configuration. As the channel begins to incline slightly in the transverse direction, the transverse rolls become unstable whereas the longitudinal rolls maintain their stability appearing to become slightly more stable as the angle increases. For the Up Hexagons, both type 1 and type 2 are unstable initially, around $\chi \approx 1°$ the eigenvalues begin to decrease until they become stable at approximately $\chi \approx 1.1°$ and $\chi \approx 1.2°$ respectively. The down hexagons for both type 1 and type 2 are stable and remain stable for the small increase in angle.

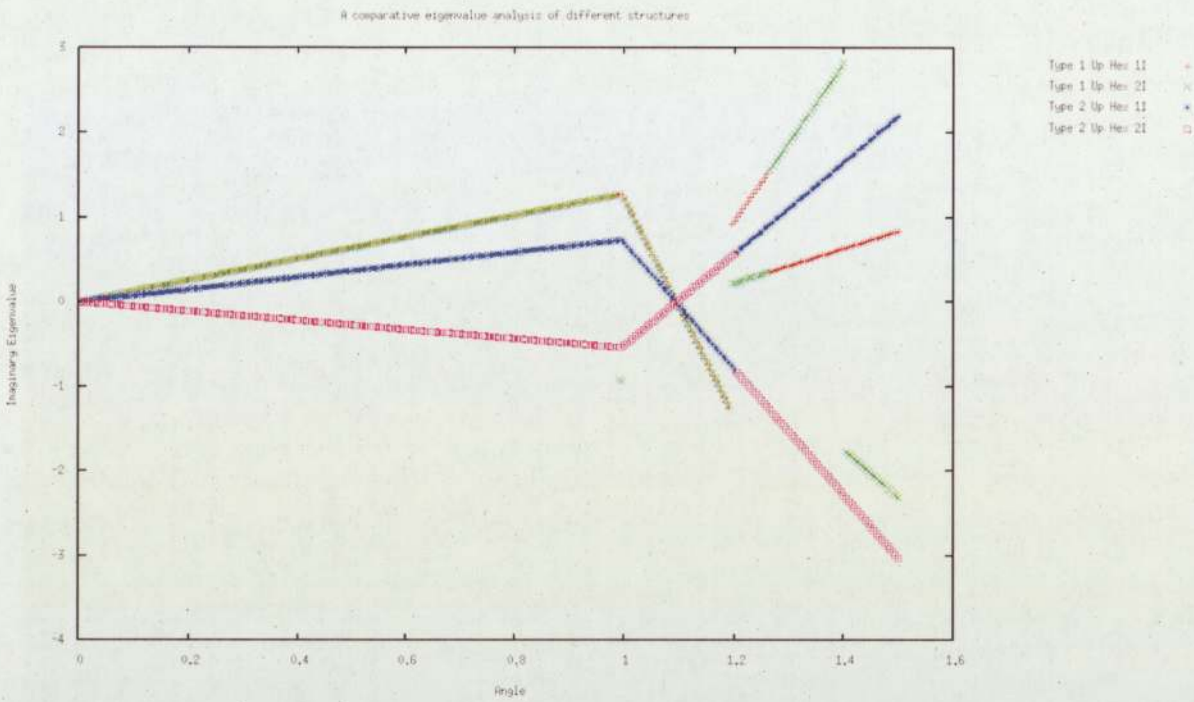

Figure 5.6: Imaginary Eigenvalues against a small angle variation for Air (Pr = 0.705). A disturbance (d, b) is applied to the structures such that: Type 1 Up Hex $(1.14, 0.66)$; Type 2 Up Hex (0.66,1.14).

For the imaginary eigenvalue analysis we split the structures into groups. Figure 5.5 illustrates a significant trend for the transverse rolls, the first imaginary eigenvalue σ_i remains constant whereas the second σ_i shows a significant declining trend, this suggests the transverse roll is a travelling wave. On the other hand the longitudinal rolls show no significant trend perhaps suggesting they are stationary waves.

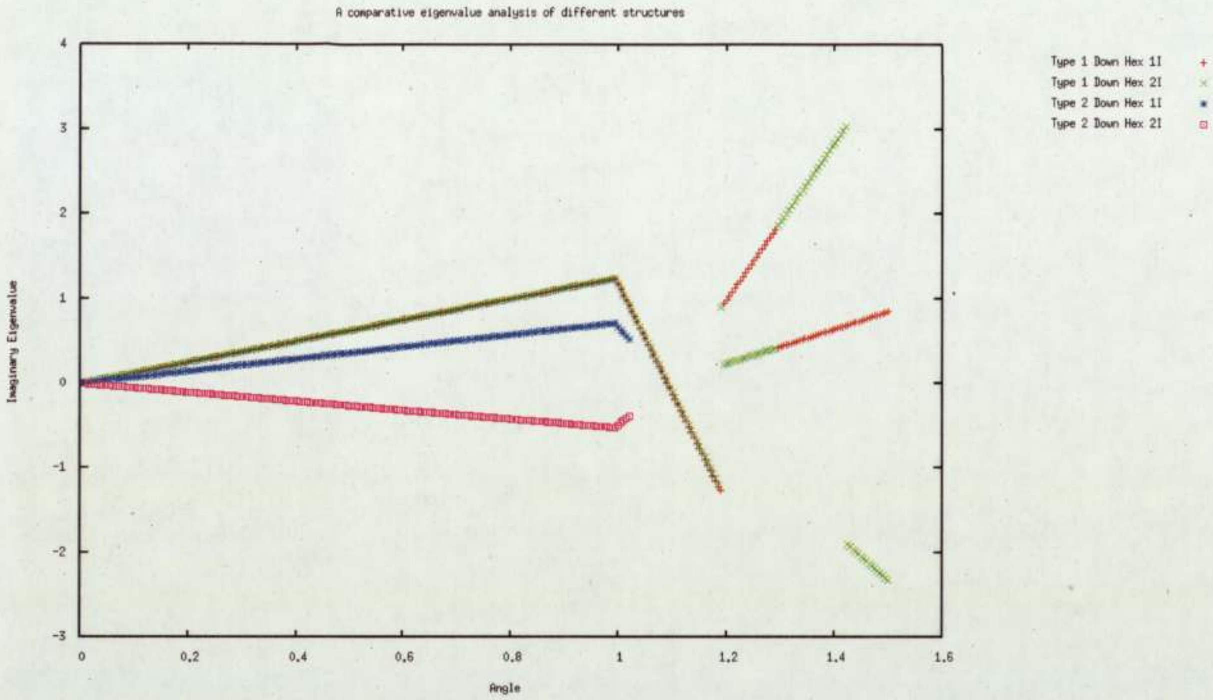

Figure 5.7: Imaginary Eigenvalues against a small angle variation for Air (Pr = 0.705). A disturbance (d, b) is applied to the structures such that: Type 1 Down Hex $(1.14, 0.66)$; Type 2 Down Hex (0.66,1.14).

In Figure 5.6 it is difficult to deduce a significant trend for the type 1 up hexagons. However for the type 2 up hexagons, the two imaginary eigenvalues has the same magnitude but opposite signs such that $|\sigma_{1i}| = -|\sigma_{2i}|$ this suggests this structure is oscillating. This result is also the case for the type 1 and type 2 down hexagonal structures, shown in Figure 5.7.

5.3.2 Stability Analysis Mercury (Pr = 0.025)

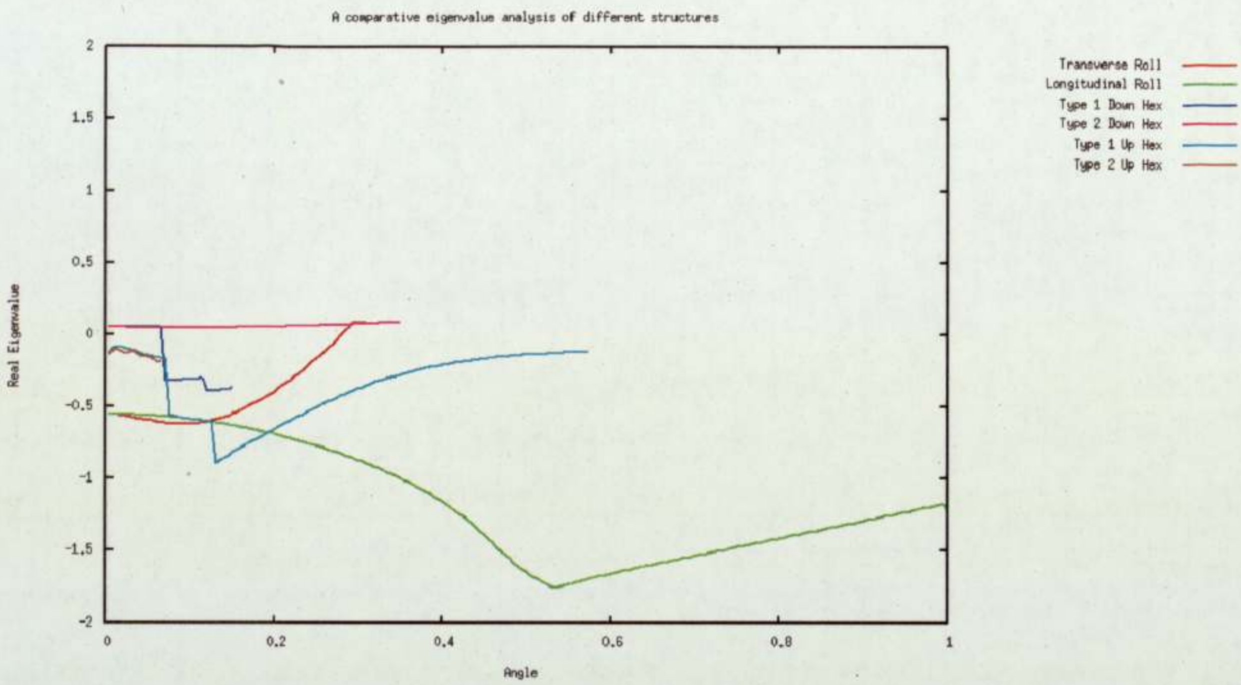

Figure 5.8: Real Eigenvalues against a small angle variation for Mercury (Pr = 0.025). For each structural type a disturbance (d, b) is applied such that: Transverse roll $(0, 1.315)$; Longitudinal roll $(1.315, 0)$; Type 1 Up/Down Hex $(1.14, 0.66)$; Type 2 Up/Down Hex (0.66,1.14).

When analysing the stability of Mercury, our first observation is that the different structures are more unpredictable in comparison to the case for Air. Nonetheless, we can deduce that the roll structures are both stable when $\chi = 0°$ but then the transverse roll becomes unstable with an extremely small angle whereas the longitudinal rolls remain stable. The up hexagons remain stable regardless of the structure type. The down hexagons however are both unstable where the type one hexagon becomes stable after an angular increase of $\chi \approx 0.05°$. For a very small Prandtl number such as Mercury, a very small change in incline can have significant effects on the stability, suggesting this fluid is notably more unstable than the case for Air.

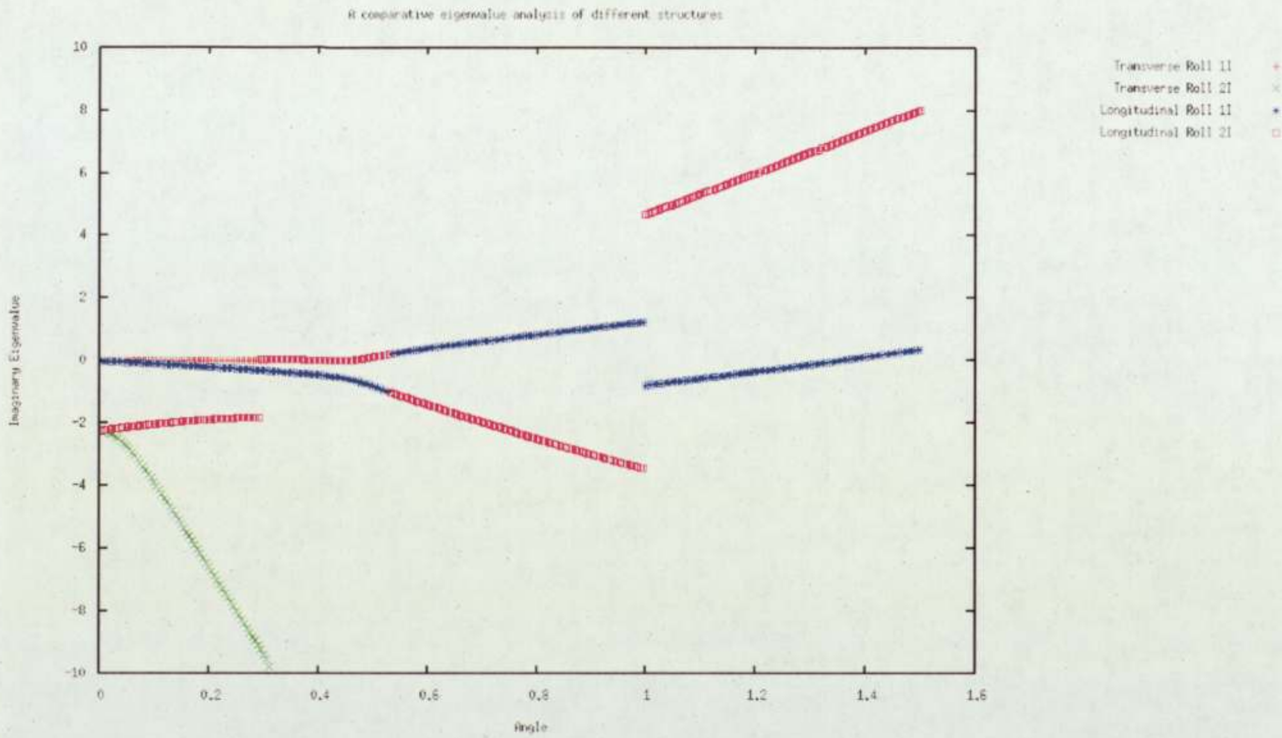

Figure 5.9: Imaginary Eigenvalues against a small angle variation for Mercury (Pr = 0.025). A disturbance (d, b) is applied to the structures such that: Transverse roll $(0, 1.315)$; Longitudinal roll $(1.315, 0)$.

For the roll structures shown in Figure 5.9, the transverse rolls for Mercury behave in a similar manner to those for Air, as one σ_i is constant and one is significantly decreasing we suggest they are travelling waves. The longitudinal rolls appear to behave in an oscillatory manner up until $\chi \approx 0.5$ however after this point we assume they are just moving waves as the eigenvalue trend is not conclusive.

The nature of the imaginary eigenvalues for the up hexagons in Figure 5.10 does not yield conclusive results for us to predict the nature of the structures. This is not necessarily a disappointment as we can see from Figure 5.8 that the up hexagons are in fact stable for the small angular variations and so they are not the most interesting of states. Down hexagons on the other hand appear to be unstable when the channel is horizontal. If we look at Figure 5.11 we can conclude the type 2 hexagons exhibit oscillatory behaviour and so we can assume that when $\chi \approx 0.05°$ the unstable down hexagon is oscillating.

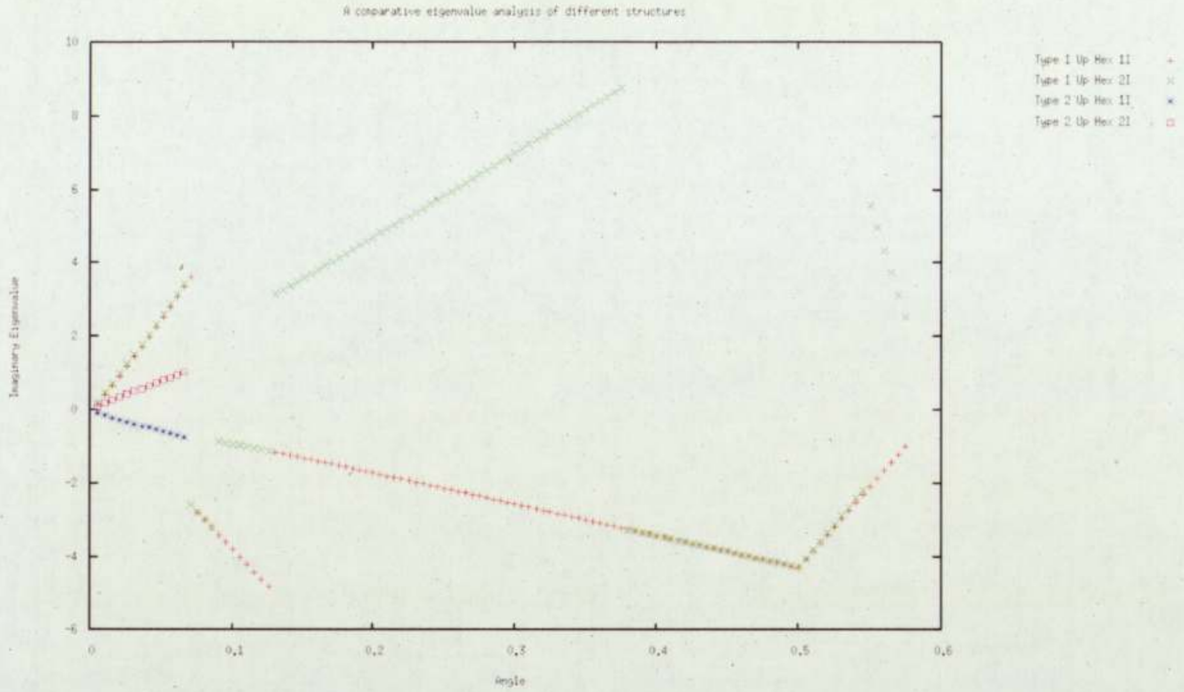

Figure 5.10: Imaginary Eigenvalues against a small angle variation for Mercury (Pr = 0.025). A disturbance (d, b) is applied to the structures such that: Type 1 Up Hex (1.14, 0.66); Type 2 Up Hex (0.66,1.14).

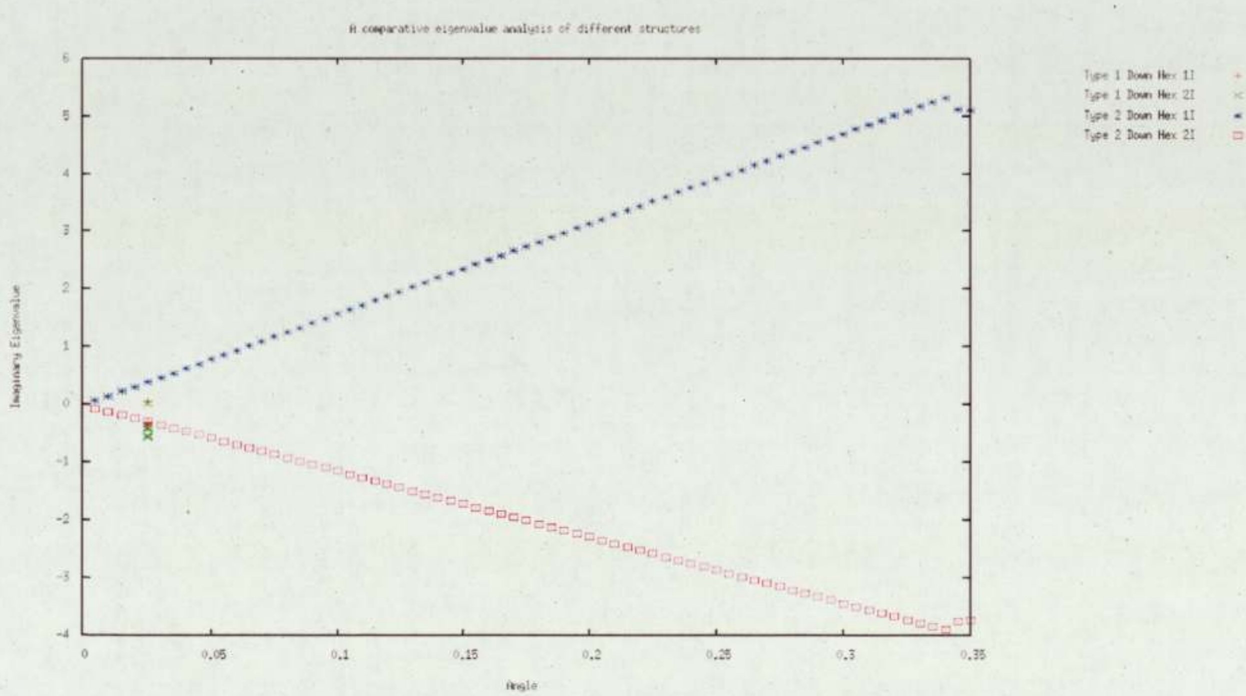

Figure 5.11: Imaginary Eigenvalues against a small angle variation for Mercury (Pr = 0.025). A disturbance (d, b) is applied to the structures such that: Type 1 Down Hex (1.14, 0.66); Type 2 Down Hex (0.66,1.14).

5.4 Stability Analysis Concluding Remarks

In the non-linear stability analysis, all of the results obtained were a conclusion of tracing the angle in our analysis. The figures, in particular the imaginary eigenvalue figures appear to have a number of jumps and overlapping of lines. We can summarise this result by assuming the overlap of the lines occur when two structures have overlapped and the dominating structure overshadows the less dominant structure. The jumps in the line segments suggest that when tracing the angle of inclination for this particular section of analysis, numerically we find solutions for different structures occurring within the same parameter space. The figures do however show some symmetry and suggested behaviour. It is evident however that the angle is not a distinguishing factor of the analysis. It may have been more productive to trace the eigenvalues for example, we could then determine the subcritical and supercritical regions of the non-linear state space.

Chapter 6

Conclusion

In this dissertation the methods and simulations described aid our analysis of modelling an internally heated fluid. The motivation of the study is to analyse a system that arises in current industrial processes. A system that emulates a corium melt pool was chosen in order to explore the convective behaviour of the fluid under the extreme conditions found within a nuclear reactor.

The understanding required in order to define and study the problem, entailed in-depth learning of fluid dynamics and more specifically the Navier Stokes equation. During this process the work of (Glover et al., 2013) and (Generalis and Nagata, 2003) inspired the direction of the research as the model studied shares similar concepts these papers. We study an internally heated system with an isothermal upper boundary and an adiabatic lower boundary. This system is then analysed when the angle of the channel is increased and when varying the control parameters.

By narrowing our analysis to three fluid materials (Air, Mercury, Water), we firstly obtained linear neutral curves showing the boundary between laminar and convection for the corresponding Prandtl values of our fluids. It was found that by changing the control parameters we find regions where the fluid exhibits different convective behaviour. When the Reynolds number is increased the critical Grashof number also increases, therefore the boundary between laminar flow and convection is found at higher Grashof values. This suggests the state of the fluid is stable for a larger range of values.

When we simultaneously increase the angle of the channel and the Reynolds number, we see that the critical Grashof number again increases. However this is only the case for small Reynolds values and inclination. As these values increase the fluids generally become unstable for all structures with the exception of the longitudinal rolls.

The most interesting part of the research was delving into the non-linear analysis of our problem. This proved to be the more challenging area of the research as the computational programs took a long time to understand and adapt for the constraints applied for this model. The execution of the programs for each parameter variation proved to be very time consuming. However the non-linear results of our study produce some interesting results for our analysis. In particular, when the angle of inclination is increased such that $\chi \approx 1^\circ$ for Air and $\chi \approx 0.005^\circ$ for Mercury, there is a region where both the up and down hexagons are in a stable state. This behaviour of the up and down hexagonal structures have rarely been found (Groh et al., 2007). This warrants the motivation to further the non-linear study of this system to perhaps see if this behaviour occurs for different Prandtl or Reynolds values.

Appendices

Appendix A

Non-dimensionalisation

This appendix is an extension of section 2.1.2. In order to simplify our calculations corresponding to the modelled problem, we non-dimensionalise our governing equations to remove all dimensional units. This allows our problem to be more widely used as we can rescale our problem and results with respect to specific parameters. A method on how we can normalise our parameters to substitute into our governing equations is explained in section 2.1.2. We begin by introducing the dimensional governing equations. Note the asterisk represents the dimensional variables.

$$\frac{\partial \mathbf{u}^*}{\partial t^*} + \mathbf{u}^* \cdot \nabla^* \mathbf{u}^* = -\frac{1}{\rho}\nabla^* \pi^* + \nu^* \nabla^{2*}\mathbf{u}^* - g\gamma(T - T_r), \tag{A.1}$$

$$\frac{\partial T^*}{\partial t^*} + \mathbf{u}^* \cdot \nabla^* T^* = \kappa \nabla^{2*} T^* + q, \tag{A.2}$$

$$\nabla^* \cdot \mathbf{u}^* = 0. \tag{A.3}$$

We now need to define our variables and spatial derivatives in terms of the reference constant and substitute into equations (A.1) - (A.3).

$$\begin{array}{lclclcl}
L^* & \to & \mathrm{dL} & \quad & \nabla^{2*} & \to & \frac{1}{d^2}\nabla^2 \\
\mathbf{u}^* & \to & \frac{\nu}{d}\mathbf{u} & & \frac{\partial}{\partial t^*} & \to & \frac{\nu}{d^2}\frac{\partial}{\partial t} \\
t^* & \to & \frac{d^2}{\nu}t & & T^* & \to & \frac{qd^2}{2\kappa G_r}T \\
\nabla^* & \to & \frac{1}{d}\nabla & & \pi^* & \to & \frac{\rho\nu^2}{d^2}\pi
\end{array}$$

By substituting all of the r.h.s terms into (A.1) - (A.3) we can simplify each term to achieve the non-dimensionalised equations in section 2.1.2.

Appendix B

Derivation of δ, ϵ and $\nabla \cdot u = 0$

Delta-Epsilon Operators

We begin by defining $\boldsymbol{\epsilon}$.

$$
\begin{aligned}
\boldsymbol{\epsilon} &= \nabla \times \hat{k}, \\
&= \begin{vmatrix} \hat{i} & \hat{j} & \hat{k} \\ \partial_x & \partial_y & \partial_z \\ 0 & 0 & 1 \end{vmatrix}, \\
&= \hat{i}\left(\partial_y - \partial_z(0)\right) - \hat{j}\left(\partial_x - \partial_z(0)\right) + \hat{k}\left(\partial_x(0) - \partial_y(0)\right), \\
&= \partial_y \hat{i} - \partial_x \hat{j} + (0)\hat{k}.
\end{aligned}
$$

$$\therefore \quad \boldsymbol{\epsilon} = \left(\partial_y, -\partial_x, 0\right).$$

Following this we define $\boldsymbol{\delta}$

$$
\begin{aligned}
\boldsymbol{\delta} &= \nabla \times (\nabla \times \hat{k}), \\
&= \nabla \times \boldsymbol{\epsilon}, \\
&= \begin{vmatrix} \hat{i} & \hat{j} & \hat{k} \\ \partial_x & \partial_y & \partial_z \\ \partial_y & -\partial_x & 0 \end{vmatrix}, \\
&= \hat{i}\left(\partial_y(0) - \partial_z\partial_x\right) - \hat{j}\left(\partial_x(0) - \partial_z\partial_y\right) + \hat{k}\left(-\partial_x^2 + \partial_y^2\right), \\
&= \partial_z\partial_x \hat{i} - \partial_y\partial_z \hat{j} + (-\Delta_2)\hat{k}.
\end{aligned}
$$

$$\therefore \quad \boldsymbol{\delta} = (\partial_z\partial_x, \partial_y\partial_z, -\Delta_2)\,.$$

Now we show that $\boldsymbol{\delta} \cdot \boldsymbol{\epsilon} = 0$.

$$\begin{aligned}
\boldsymbol{\delta} \cdot \boldsymbol{\epsilon} &= \begin{pmatrix} \partial_y \\ -\partial_x \\ 0 \end{pmatrix} \cdot \begin{pmatrix} \partial_x\partial_z \\ \partial_y\partial_z \\ -\Delta_2 \end{pmatrix}, \\
&= \partial_y\partial_x\partial_z - \partial_y\partial_x\partial_z + (0)\Delta_2, \\
&= 0.
\end{aligned}$$

Incompressibility condition

The next step is to show $\nabla \cdot \mathbf{u} = 0$.

$$\begin{aligned}
\nabla \cdot \mathbf{u} &= \partial_i u_i \quad \text{for } i = 1, 2, 3, \\
&= \partial_x u_1 + \partial_y u_2 + \partial_z u_3,
\end{aligned}$$

where u_1, u_2, u_3 are the x, y, z-components of $\mathbf{u}$. We can define $\mathbf{u}$ as $\mathbf{u} = \delta\phi + \epsilon\psi$. From this definition we can define each component as:

$$\mathbf{u}_i = \delta_i\phi + \epsilon_i\psi.$$

Such that,

$$u_1 = \delta_1\phi + \epsilon_1\psi = \partial_z\partial_x\phi + \partial_y\psi,$$

$$u_2 = \delta_2\phi + \epsilon_2\psi = \partial_y\partial_z\phi - \partial_x\psi,$$

$$u_3 = \delta_3\phi + \epsilon_3\psi = -\Delta\phi.$$

Therefore,

$$
\begin{aligned}
\nabla \cdot \mathbf{u} &= \partial_x u_1 + \partial_y u_2 + \partial_z u_3, \\
&= \partial_x(\partial_z \partial_x \phi + \partial_y \psi) + \partial_y(\partial_y \partial_z \phi - \partial_x \psi) + \partial_z(-\Delta \phi), \\
&= \partial_x^2 \partial_z \phi + \partial_x \partial_y \psi + \partial_y^2 \partial_z \phi - \partial_x \partial_y \psi - \partial_z \Delta_2 \phi, \\
&= \partial_x^2 \partial_z \phi + \partial_y^2 \partial_z \phi - \partial_z \Delta_2 \phi, \\
&= \partial_z(\partial_x^2 \phi + \partial_y^2 \phi - \Delta_2 \phi), \\
&= \partial_z(\Delta_2 \phi - \Delta_2 \phi), \\
&= \partial_z(0), \\
&= 0.
\end{aligned}
$$

So we can conclude $\nabla \cdot \mathbf{u} = 0 \; \forall \; \mathbf{u}$ given $\boldsymbol{\delta}$ and $\boldsymbol{\epsilon}$.

Appendix C

Derivation of computable equations

This appendix is an extension of section 3.2 where we explain the process of preparing the governing equations so that they can be implemented computationally. As explained for this to occur it is necessary to apply the $\boldsymbol{\delta}$, $\boldsymbol{\epsilon}$ operators to equation (3.10). The most simple way to do this is to apply the operators term by term. In this appendix we will demonstrate the result of applying the operators on a number of terms, when these results are applied to all terms and then put together, we obtain the computable equations.

$\boldsymbol{\epsilon}$ - operator

$\boldsymbol{\epsilon} \cdot \frac{\partial \hat{\mathbf{u}}}{\partial t}$

$$\begin{aligned}
\boldsymbol{\epsilon} \cdot \left(\frac{\partial \hat{\mathbf{u}}}{\partial t}\right) &= \boldsymbol{\epsilon} \cdot \frac{\partial}{\partial t}(\boldsymbol{\delta}\phi + \boldsymbol{\epsilon}\psi), \\
&= \frac{\partial}{\partial t}\boldsymbol{\epsilon}(\boldsymbol{\delta}\phi + \boldsymbol{\epsilon}\psi), \\
&= \frac{\partial}{\partial t}(\epsilon_i)^2\psi, \\
&= \frac{\partial}{\partial t}(\partial_y^2 + \partial_x^2)\psi, \\
&= \frac{\partial}{\partial t}\Delta_2\psi.
\end{aligned}$$

$\boldsymbol{\epsilon} \cdot \nabla \pi$

$$\begin{aligned}
\boldsymbol{\epsilon} \cdot \nabla \pi &= \begin{pmatrix} \partial_y \\ -\partial_x \\ 0 \end{pmatrix} \cdot \begin{pmatrix} \partial_x \pi \\ \partial_y \pi \\ \partial_z \pi \end{pmatrix}, \\
&= \partial_y \partial_x \pi - \partial_x \partial_y \pi + (0)\partial_z \pi, \\
&= (\partial_y \partial_x - \partial_x \partial_y)\pi, \\
&= (0)\pi, \\
&= 0.
\end{aligned}$$

$\boldsymbol{\epsilon} \cdot (\hat{k} \cos \chi + \hat{i} \sin \chi)\theta$

$$\begin{aligned}
\boldsymbol{\epsilon} \cdot (\hat{k} \cos \chi + \hat{i} \sin \chi)\theta &= \epsilon_3 \theta \cos \chi + \epsilon_1 \theta \sin \chi, \\
&= 0 + \partial y \theta \sin \chi.
\end{aligned}$$

$\boldsymbol{\epsilon} \cdot ((\hat{\mathbf{u}} \cdot \nabla)\mathbf{u})$

$$\begin{aligned}
\boldsymbol{\epsilon} \cdot ((\hat{\mathbf{u}} \cdot \nabla)\mathbf{u} &= \epsilon_1 \cdot ((\hat{\mathbf{u}} \cdot \nabla)u_1 + \epsilon_2 \cdot ((\hat{\mathbf{u}} \cdot \nabla)u_2 + \epsilon_3 \cdot ((\hat{\mathbf{u}} \cdot \nabla)u_3, \\
&= \epsilon_1 (\hat{\mathbf{u}} \cdot \nabla)u_1, \\
&= \epsilon_1 (u_i \partial_i) U_0(z) \\
&= \epsilon_1 (u_1 \partial_x + u_2 \partial_y + u_3 \partial_z) U_0(z), \\
&= \epsilon_1 (u_3 \partial_z U_0(z)), \\
&= \partial_y ((\delta_3 \phi + \epsilon_3 \psi)\partial_z) U_0(z), \\
&= \partial_y ((\delta_3 \phi)\partial_z) U_0(z), \\
&= \partial_y ((-\Delta_2 \phi)\partial_z) U_0(z), \\
&= -\partial_3 U_0(z) \Delta_2 \partial_2 \phi.
\end{aligned}$$

$\boldsymbol{\epsilon} \cdot ((\mathbf{u} \cdot \nabla)\hat{\mathbf{u}})$

$$\begin{aligned}
\boldsymbol{\epsilon} \cdot ((\mathbf{u} \cdot \nabla)\hat{\mathbf{u}}) &= \epsilon_i(U_o(z) \cdot \nabla)u_i, \\
&= \epsilon_i(U_o(z)\partial_x)u_i, \\
&= \epsilon_1(U_o(z)\partial_x)u_1 + \epsilon_2(U_o(z)\partial_x)u_2 + \epsilon_3(U_o(z)\partial_x)u_3, \\
&= \epsilon_1(U_o(z)\partial_x)u_1 + \epsilon_2(U_o(z)\partial_x)u_2 + \epsilon_3(U_o(z)\partial_x)u_3, \\
&= \epsilon_1(U_o(z)\partial_x)(\delta_1\phi + \epsilon_1\psi) + \epsilon_2(U_o(z)\partial_x)(\delta_2\phi + \epsilon_2\psi) + \epsilon_3(U_o(z)\partial_x)(\delta_3\phi + \epsilon_3\psi), \\
&= \epsilon_1(U_o(z)\partial_x)\left[\partial_z\partial_x\phi + \partial_y\psi\right] + \epsilon_2(U_o(z)\partial_x)\left[\partial_y\partial_z\phi - \partial_x\psi\right] + \epsilon_3(U_o(z)\partial_x)\left[-\Delta_2\phi\right], \\
&= (U_o(z)\partial_x)\partial_y\left[\partial_z\partial_x\phi + \partial_y\psi\right] - (U_o(z)\partial_x)\partial_x\left[\partial_y\partial_z\phi - \partial_x\psi\right], \\
&= (U_o(z)\partial_x)\left[(\partial_x^2 + \partial_y^2)\psi\right], \\
&= U_o(z)\partial_x\Delta_2\psi.
\end{aligned}$$

$\boldsymbol{\epsilon} \cdot (\nabla^2\mathbf{u})$

$$\begin{aligned}
\boldsymbol{\epsilon} \cdot \nabla^2\mathbf{u} &= \nabla^2\boldsymbol{\epsilon} \cdot \mathbf{u}, \\
&= \nabla^2\boldsymbol{\epsilon}(\boldsymbol{\delta}\phi + \boldsymbol{\epsilon}\psi), \\
&= \nabla^2(\epsilon_i)^2\psi, \\
&= \nabla^2(\partial_y^2 + \partial_x^2)\psi, \\
&= \nabla^2\Delta_2\psi.
\end{aligned}$$

$\boldsymbol{\delta}$ - operator

$\boldsymbol{\delta} \cdot \frac{\partial \mathbf{u}}{\partial t}$

$$
\begin{aligned}
\boldsymbol{\delta} \cdot \left(\frac{\partial \mathbf{u}}{\partial t}\right) &= \boldsymbol{\delta} \cdot \frac{\partial}{\partial t}(\boldsymbol{\delta}\phi + \boldsymbol{\epsilon}\phi), \\
&= \frac{\partial}{\partial t}(\boldsymbol{\delta}(\boldsymbol{\delta}\phi + \boldsymbol{\epsilon}\phi)), \\
&= \frac{\partial}{\partial t}(\delta_i)^2\phi \\
&= \frac{\partial}{\partial t}[\partial_x^2\partial_z^2 + \partial_y^2\partial_z^2 + \Delta_2^2]\phi, \\
&= \frac{\partial}{\partial t}[\Delta_2\partial_z^2 + \Delta_2\Delta_2]\phi, \\
&= \frac{\partial}{\partial t}[\Delta_2(\partial_z^2 + \Delta_2)]\phi, \\
&= \frac{\partial}{\partial t}(\Delta_2\nabla^2)\phi.
\end{aligned}
$$

$\boldsymbol{\delta} \cdot \nabla\pi$

$$
\begin{aligned}
\boldsymbol{\delta} \cdot \nabla\pi &= \begin{pmatrix} \partial_x\partial z \\ \partial_y\partial_z \\ -\Delta_2 \end{pmatrix} \cdot \begin{pmatrix} \partial_x\pi \\ \partial_y\pi \\ \partial_z\pi \end{pmatrix}, \\
&= \partial_x\partial_z\partial_x\pi + \partial_y\partial_z\partial_y\pi - \Delta_2\partial_z\pi, \\
&= (\partial_x\partial_z\partial_x + \partial_y\partial_z\partial_y - \Delta_2)\pi, \\
&= (\partial_z(\partial_x\partial_x + \partial_y\partial_y - \Delta_2)\pi, \\
&= (\partial_z(\partial_x^2 + \partial_y^2 - \Delta_2)\pi), \\
&= (\partial_z(\Delta_2 - \Delta_2)\pi), \\
&= \partial_z(0)\pi, \\
&= 0.
\end{aligned}
$$

$\boldsymbol{\delta} \cdot (\hat{k}\cos\chi + \hat{\imath}\sin\chi)\theta$

$$
\begin{aligned}
\boldsymbol{\delta} \cdot (\hat{k}\cos\chi + \hat{\imath}\sin\chi)\theta &= \delta_3\theta\cos\chi + \delta_1\theta\sin\chi, \\
&= -\Delta_2\theta\cos\chi + \partial x\partial z\theta\sin\chi.
\end{aligned}
$$

$\boldsymbol{\delta} \cdot \nabla^2 \hat{\mathbf{u}}$

$$
\begin{aligned}
\boldsymbol{\delta} \cdot \nabla^2 \hat{\mathbf{u}} &= \nabla^2 \boldsymbol{\delta} \cdot \hat{\mathbf{u}}, \\
&= \nabla^2 \boldsymbol{\delta}(\boldsymbol{\delta}\phi + \epsilon\phi), \\
&= \nabla^2 (\delta_i)^2 \cdot \phi \\
&= \nabla^2 \left[\partial_x^2 \partial_z^2 + \partial_y^2 \partial_z^2 - \Delta_2^2\right] \phi, \\
&= \nabla^2 \left[\Delta_2 \partial_z^2 + \Delta_2 \Delta_2\right] \phi, \\
&= \nabla^2 \left[\Delta_2 (\partial_z^2 + \Delta_2)\right] \phi, \\
&= \nabla^2 (\Delta_2 \nabla^2) \phi.
\end{aligned}
$$

Bibliography

F. J. Asfia and V. K. Dhir. Nuclear engineering and design. *An experimental study of natural convection in a volumetricallu heated sperical pool bounded on top with a rigid wall*, 163:333–348, 1996.

G. K. Batchelor. *An introduction to fluid dynamics.* Cambridge University Press, 1967.

Chandrasekhar. *Hydrodynamic and hydromagnetic stability.* Dover Publications : New York, 1981.

R. M. Clever. Heat transfer and stability properties of convection rolls in an internally heated fluid layer. *Applied Mathematics and Physics*, 28:585–597, 1977.

S. C. Generalis and M. Nagata. Transition in homogeneously heated inclined plane parallel shear flows. *Journal of Heat Transfer*, 125:795–803, 2003.

G. M. Cartland Glover, K. Fujimura, and S. C. Generalis. Effect of aspect ratio on thermal convection in open and closed systems. In *The 15th International Topical Meeting On Nuclear Reactor Thermal - Hydraulics*, Italy, May 2013.

C. Groh, R. Richter, I. Rehberg, and F. H. Busse. Reorientation of a hexagonal pattern under broken symmetry: The hexagon flip. *The American Physical Society*, 76, 2007.

P A Kuchment. Floquet theory for partial differential equations. *Russian Mathematical Surveys*, 37(4), 1982. URL `http://stacks.iop.org/0036-0279/37/i=4/a=R01`.

R. K. Mohanty, S. Karaa, and U. Arora. Arithmetic average discretization for the solution of 1-d nonlinear parabolic equations. *Numerical Methods for Partial Differential Equations*, 23:640–651, 2007.

M. Nagata and S. C. Generalis. Transition in convective flows heated internally. *Journal of Heat Transfer*, 124:635–642, 2002.

J. F. Price. Lagrangian and eulerian representations of fluid flow: Kinematics and the equations of motion. 2006. URL `http://www.whoi.edu/science/PO/people/jprice`.

G. Schubert, D. L. Turcotte, and P. Olson. *Mantle convection in the Earth and Planets*. Cambridge University Press, 2001.

J. Takahashi, Y. Tasaka, Y. Murai, Y. Takeda, and T. Yanagisawa. Experiemental study of cell pattern formation induced by internal heat sources in a horizontal fluid layer. *International Journal of Heat and Mass Transfer*, 53:1483–1490, 2010.

D. J. Tritton and M. N. Zarraga. Convection in horizontal layers with internal heat. experiemnts. *Journal of Fluid Mechanics*, 30:22–31, 1967.

M. Tveitereid and E. Palm. Convection due to internal heat sources. *Journal of Fluid Mechanics*, 76:481–499, 1976.

R.Kh. Zeytounian. Joseph boussinesq and his approximation: a contemporary view. *ditions scientifiques et medicales Elsevier SAS*, 331:575–586, 2003.

D. G. Zill, F. R. Marotto, and S. Generalis. *ODEs, multivariate calculus and chaos*. Brooks Cole Cengage Learning, 2009.

Further Reading

J. Boussinesq. Theorie analytique de la chaleur: Avec la thermodynamique. *de physique Mathematique de la faculte des sciences*, 1903.

R. C. Briant and A. M. Weinberg. Moulten florides as power reactor fuels. *Nuclear Science and Engineering*, 2:797–803, 1957.

P. G. Drazin and W. H. Reid. *Hydrodynamic Stability*. Cambridge University Press, 2 edition, 2004.

G. M. Cartland Glover and S. C. Generalis. Engineering applications of computational fluid mechanics. *Pattern competition in homogeneously heated fluid layers*, 3:164–174, 2009.

A. Horvat, I. Kljenak, and J. Marn. Dynamics of heat transfer in the melt pool at nuclear severe accident conditions. In *The 9th International Topical Meeting On Nuclear Reactor Thermal - Hydraulics*, California, October 1999.

P. H. Roberts. Convection in horizontal layers with internal heat generation. theory. *Journal of Fluid Mechanics*, 30:33–49, 1967.

D. J. Tritton. Journal of fluid mechanics. *Note on the effect of a nearby obstacle on turbulence intensity in a boundary layer*, 28:433–437, 1967.

R.Kh. Zeytounian and C. R. Mecanique. Lagrangian and eulerian representations of fluid flow: Kinematics and the equations of motion. *ditions scientifiques et medicales Elsevier SAS*, 331:575–586, 2003.